Journal of Constructional Steel Research 240 (2026) 110254

Contents lists available at ScienceDirect

Journal of Constructional Steel Research

journal homepage: www.elsevier.com/locate/jcsr

Hysteretic behavior of a tandem self-centering double-stage yielding buckling-restrained brace☆

Yongkang Kang [a], Bo Wen [a,b,*], Shuaishuai Ji [a], Alessio Fumagalli [c], Zhengyao Yu [a], Wen Xia [a]

[a] School of Civil Engineering, Xi'an University of Architecture and Technology, No. 13, Yanta Road, Xi'an 710055, China
[b] Key Lab of Structural Engineering and Earthquake Resistance, Ministry of Education (XAUAT), No. 13, Yanta Road, Xi'an 710055, China
[c] Department of Mathematics, Politecnico di Milano, p.za Leonardo da Vinci 32, Milano 20133, Italy

ARTICLE INFO

Keywords:
Self-centering
Buckling-restrained brace
Double-stage yielding
Restoring-force model
Finite element model
Hysteretic behavior

ABSTRACT

This paper proposes a tandem self-centering double-stage yielding buckling-restrained brace (TSCDY-BRB). A staged-stiffness restoring-force model and a three-dimensional finite element model are developed and validated against quasi-static tests, and reproduce the hysteretic response within about 15% error. The brace exhibits stable flag-shaped hysteresis, transitioning from a single-flag loop at small drifts to a flag with a second yielding plateau after the Group-2 cores engage. Parametric studies indicate that prestress sets the strength baseline and controls recentering; strand diameter influences post-activation stiffness; the Group-1 core area dictates initial strength, stiffness and low-amplitude energy dissipation; the Group-2 core area governs Stage II strength, stiffness and high-amplitude dissipation; and a larger preset gap delays Stage II activation, improving recentering but reducing damping. Within the studied range, single-cycle energy dissipation reaches 6.5–10.5 kJ, with an equivalent viscous damping ratio of 0.12–0.17, and the residual-to-peak displacement ratio remains below 3% with suitable prestress and gap. For design, an initial prestress about 1.5 times the combined yield force of the two core groups is recommended, and the preset engagement gap and the yield displacement of the Group-2 cores should be coordinated with the target peak displacement to ensure effective recentering and staged energy dissipation. System-level analysis of a six-story steel frame shows that, compared with a double-stage yielding BRB frame of identical initial properties, the TSCDY-BRB frame achieves much smaller residual drifts while maintaining comparable peak drifts under 0.2 g and 0.4 g excitations, confirming its effectiveness over different seismic levels.

1. Introduction

Conventional buildings can experience notable residual drift after strong earthquakes, and repair costs are high, which conflicts with rapid functional recovery [1,2]. Passive energy-dissipation devices are therefore widely used. Among them, buckling-restrained braces (BRBs) are popular for their stable, repeatable hysteresis; however, the yielding core still accumulates plasticity and leaves residual drift [3–5].

To limit residual deformation while retaining energy dissipation, self-centering (SC) elements are placed in parallel with dissipative components to produce a flag-shaped response. Christopoulos et al. [6] proposed and validated the self-centering energy-dissipative bracing (SC-EDB) concept at component and frame scales. Erochko et al. [7] conducted shake-table tests of SC-braced frames and reproduced the response numerically. For SC-BRBs with metallic cores, subsequent studies established trilinear hysteresis and provided design-oriented formulations, including displacement evaluation under trilinear behavior and design-load selection for first and subsequent loading [8,9]. Other SC solutions include SMA-based BRBs [10], cross-anchored dual-core self-centering braces [11], low-prestress strategies [12], disc-spring SC braces and compounded layouts verified by mechanics and cyclic tests [13,14], and pre-pressed disc-spring SC braces with clarified cyclic behavior and failure mechanisms [15,16]. Assembled SC-BRBs showed high post-yield stiffness and replaceability in component and application studies [17,18]. Additional mechanisms include an embedded-friction-spring SC brace [19], a self-centering friction damper

☆ This article is part of a Special issue entitled: 'Self-centering Struct' published in Journal of Constructional Steel Research.

* Corresponding author.
E-mail addresses: kangykxy@163.com (Y. Kang), wenbo_mail@163.com (B. Wen), 1620563726@qq.com (S. Ji), alessio.fumagalli@polimi.it (A. Fumagalli), yuzhengyao@xauat.edu.cn (Z. Yu), xw18137287486@163.com (W. Xia).

https://doi.org/10.1016/j.jcsr.2026.110254
Received 27 September 2025; Received in revised form 29 December 2025; Accepted 17 January 2026
Available online 29 January 2026

with confined SMA bars [20], viscous damper and a disc-spring variants [21,22], a coaxially formed SC-BRB verified experimentally [23], and variable damping SC braces [24]. More recently, Hu et al. [25] developed hybrid self-centering braces combining SMA U-shaped dampers and rate-dependent viscoelastic dampers, and demonstrated through validation tests and system-level analyses that such braces can simultaneously control peak and residual drifts as well as floor accelerations of multistory steel frames.

Performance-based design also requires matching resistance across hazard levels. For frequent events, nonstructural damage should be limited; for rare events, higher strength and dissipation should engage. To this end, staged or multilevel yielding has been developed, including segmented cores, replaceable fuses, trigger mechanisms, and dual-stiffness or coupling devices. Two-level-yield BRB tests and parametric studies documented staged yielding and design implications [26–28]. Sitler et al. [29] carried out full-scale tests on a multistage BRB. Miniature dual-stiffness dampers and double-stage coupling components were proposed and evaluated by tests or simulations [30–32]. Sun et al. [33] developed and validated an assembled double-stage BRB. Hu et al. [34] designed and analyzed a cross-shaped double-stage BRB and identified key parameter effects. A shape-optimized dumbbell-type slit damper showed phased yielding and stable cyclic performance [35]. At the frame level, resilience comparisons between double-stage and conventional BRB systems were also reported [36].

Coupling staged yielding with self-centering has recently gained attention, showing the potential to combine recentering with tunable multi-stage dissipation. Zhang et al. [37] introduced and validated an assembled self-centering dual-stage yield BRB and analyzed its hysteretic behavior. Jiang et al. [38] proposed a double-activation brace using two disc-spring groups and verified frame response. Chen et al. [39] reported a self-centering brace with staged-yield dissipation that achieved full flag-shaped loops and offered design guidance, and Yang et al. [40] developed a dual-stage energy-dissipation and self-centering friction damper, further demonstrating the feasibility of the coupled concept.

On the methodology side, numerical modelling for these devices has matured. Calibrated finite element (FE) models are routinely used to study force transfer, initial and equivalent stiffness, and cyclic response, with parameters identified against tests [41–45]. System-level studies further inform performance objectives [46]. This methodological foundation supports the application of the finite element method for verification work and parameter exploration.

Building on prior research, a tandem self-centering double-stage-yielding buckling-restrained brace (TSCDY-BRB) is proposed. The brace comprises two groups of core plates that engage sequentially and a tandem tendon-bundle self-centering system, enabling Stage I and Stage II activation while preserving recentering. Compared with the aforementioned self-centering braces and double-stage yielding BRBs (DY-BRBs) without explicit self-centering, the TSCDY-BRB adopts a configuration in which the self-centering and staged-yielding subsystems are clearly separated yet coupled in parallel; the tendon-bundle branch remains active over the entire deformation range, whereas the two groups of core plates in the energy-dissipation branch are engaged at different drift levels, which facilitates design and analytical modelling. The concept and working mechanism are presented. A segment-wise restoring-force model is formulated, and a numerical model is developed in ABAQUS [47]. Both are validated against full-scale quasi-static test results. The calibrated three-dimensional FE model is then used to quantify the effects of strand prestress and diameter, the yielding-segment areas of the two core-plate groups, and the preset engagement gap of the second group on the hysteretic behavior of the TSCDY-BRB. The results establish parameter–response relationships and provide design guidance for multi-level performance objectives. In addition, nonlinear response-history analyses of a six-story steel frame equipped with TSCDY-BRBs and, for comparison, DY-BRBs are carried out to examine how the TSCDY-BRB influences peak and residual inter-story drifts at the system level.

2. Configuration and working mechanism of TSCDY-BRB

2.1. Configuration

The structural layout of the TSCDY-BRB is illustrated in Fig. 1. The brace integrates two parallel subsystems: a tandem self-centering system and a double-stage yielding energy dissipation system. The self-centering system comprises two prestressed tendon sets, an inner tube, an intermediate tube, an outer tube, and end plates. The tendon sets are threaded through the inner tube in opposite directions, each anchored at one end to an inner end plate and at the other end to the corresponding outer end plate. Prestressing keeps all tubes tightly seated against their end plates, with the inner tube suspended in a floating, non-contact position parallel to the intermediate and outer tubes. In this tandem arrangement, the two tendon sets share the total axial deformation equally, thereby increasing the overall elongation capacity.

The double-stage yielding energy dissipation system employs a staged activation scheme using T-shaped blocks and two groups of dumbbell-shaped core plates, hereafter referred to as Group-1 and Group-2. Each core plate consists of connection, transition, energy-dissipation, and free segments. The free segments contain rectangular holes aligned with corresponding openings in the outer tube; the connection segments are welded to the surface of the intermediate tube. Four plates are arranged symmetrically between the intermediate and outer tubes and grouped by the hole sizes in their free segments (two plates per group). Group-1 core plates are mounted on the top and bottom faces of the intermediate tube with their free segments oriented toward the left end; Group-2 core plates are mounted on the front and rear faces with free segments oriented toward the right end. This orthogonal arrangement ensures that the two groups exhibit complementary tension–compression yielding during bidirectional loading, as described in Section 2.2.

Each plate is flanked by constraining plates, and a buckling-restraining plate covers the assembly. Together with the intermediate tube, these components form a restraining unit that allows in-plane expansion of the plates while preventing out-of-plane buckling. Eight guide blocks are placed between the intermediate and outer tubes to reduce sliding friction. All components—including the constraining plates, buckling-restraining plates, and guide blocks—are welded to the intermediate tube.

The brace's left and right connection ends are bolted to steel attachments welded to the outer and intermediate tubes, respectively. External loads applied to these connections induce relative axial displacement between the intermediate and outer tubes, simultaneously activating both subsystems. Rectangular holes and slotted holes are machined into all faces of the outer tube: the rectangular holes serve as engagement interfaces between the T-blocks and the free segments of the core plates, while the slotted holes accommodate the axial sliding of the right connection end of the intermediate tube, thereby enabling its movement and driving the relative displacement between tubes. The T-blocks are welded to the outer tube and extend inward through the rectangular holes toward the free-segment holes of the core plates.

2.2. Working mechanism

The working principle of the TSCDY-BRB is governed by the relative axial displacement ($\Delta\delta_{rel}$) between the intermediate and outer tubes (Fig. 2), which causes the end gaps at the tube-end-plate interfaces to open at the activation threshold and to close on reverse sliding when the displacement returns to the activation value. For explanatory purposes, the left connection end is assumed fixed. Under this assumption, the outer tube and its welded T-blocks remain stationary, while axial loading applied to the right connection drives the intermediate tube to slide relative to the outer tube, triggering both self-centering and

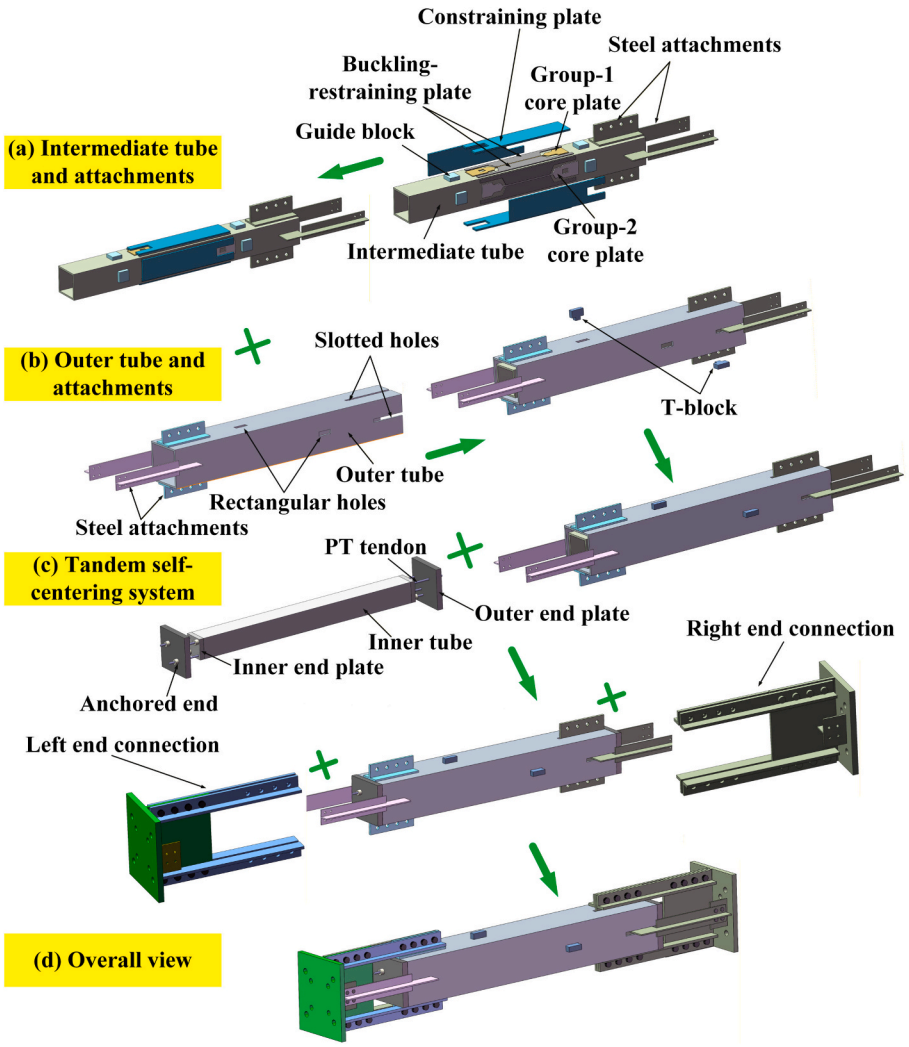

Fig. 1. Configuration of the TSCDY-BRB.

energy-dissipation mechanisms.

In this article, the two yielding stages of the TSCDY-BRB are denoted as Stage I and Stage II. In Stage I, only the Group-1 core plates yield; in Stage II, both the Group-1 and Group-2 core plates yield. The ends of each T-block are fully inserted into the rectangular holes in the free segments of both core-plate groups. In Group-1, the holes are machined for a zero-clearance fit with the T-block ends, ensuring immediate engagement: any relative displacement causes the hole walls to bear directly against the T-block ends, transferring load to the plates without delay. In Group-2, the holes incorporate a preset axial gap u between each sidewall and the corresponding face of the T-block end. This design delays engagement until $\Delta\delta_{rel}$ reaches $\pm u$, at which point one sidewall contacts the T-block end and the plates begin to carry load. Reversal of loading requires a displacement change of $2u$ to engage the opposite sidewall, ensuring a defined delay before Group-2 activation in the opposite direction.

Under tensile loading ($\Delta\delta_{rel} > 0$), the intermediate tube moves rightward. Group-1 plates yield in tension immediately due to zero clearance, whereas Group-2 plates remain inactive until $\Delta\delta_{rel}$ reaches u, at which point they yield in compression. Under compressive loading ($\Delta\delta_{rel} < 0$), the intermediate tube moves leftward, causing Group-1 plates to yield in compression immediately, and the Group-2 plates yield in tension once $\Delta\delta_{rel}$ reaches $-u$. Once Group-2 engages, both groups deform in parallel, increasing the total energy-dissipation capacity.

Upon unloading, the prestressed tendons restore $\Delta\delta_{rel}$ to zero, providing complete self-centering. The tandem tendon configuration allows the total $\Delta\delta_{rel}$ to be twice the elongation of each tendon set, enabling larger permissible deformations without exceeding tendon elastic strain limits. This ensures the stability of the energy-dissipation process and reliable post-earthquake recentering. In summary, Stage I consists of the immediate yielding of Group-1 plates, analogous to a conventional buckling-restrained braces, while Stage II begins when the displacement threshold u is reached, activating Group-2 in a complementary yielding mode. This staged activation provides graded energy dissipation and improved seismic resilience, while the prestressed tendon system maintains robust self-centering performance.

3. Theory analysis

3.1. Model overview and notation

To interpret the hysteretic behavior of the TSCDY-BRB, a simplified physical model is formulated in the assembly-end (total displacement) coordinate (Fig. 3); the total axial displacement is denoted by δ and the total restoring force by $F(\delta)$. The brace is idealized as a series system consisting of a main body and two end connections. The main body comprises a self-centering system (SCS) in parallel with two energy-dissipation subsystems (EDS-1 and EDS-2), corresponding to the Group-1 and Group-2 core plates, respectively. Consistent with Section

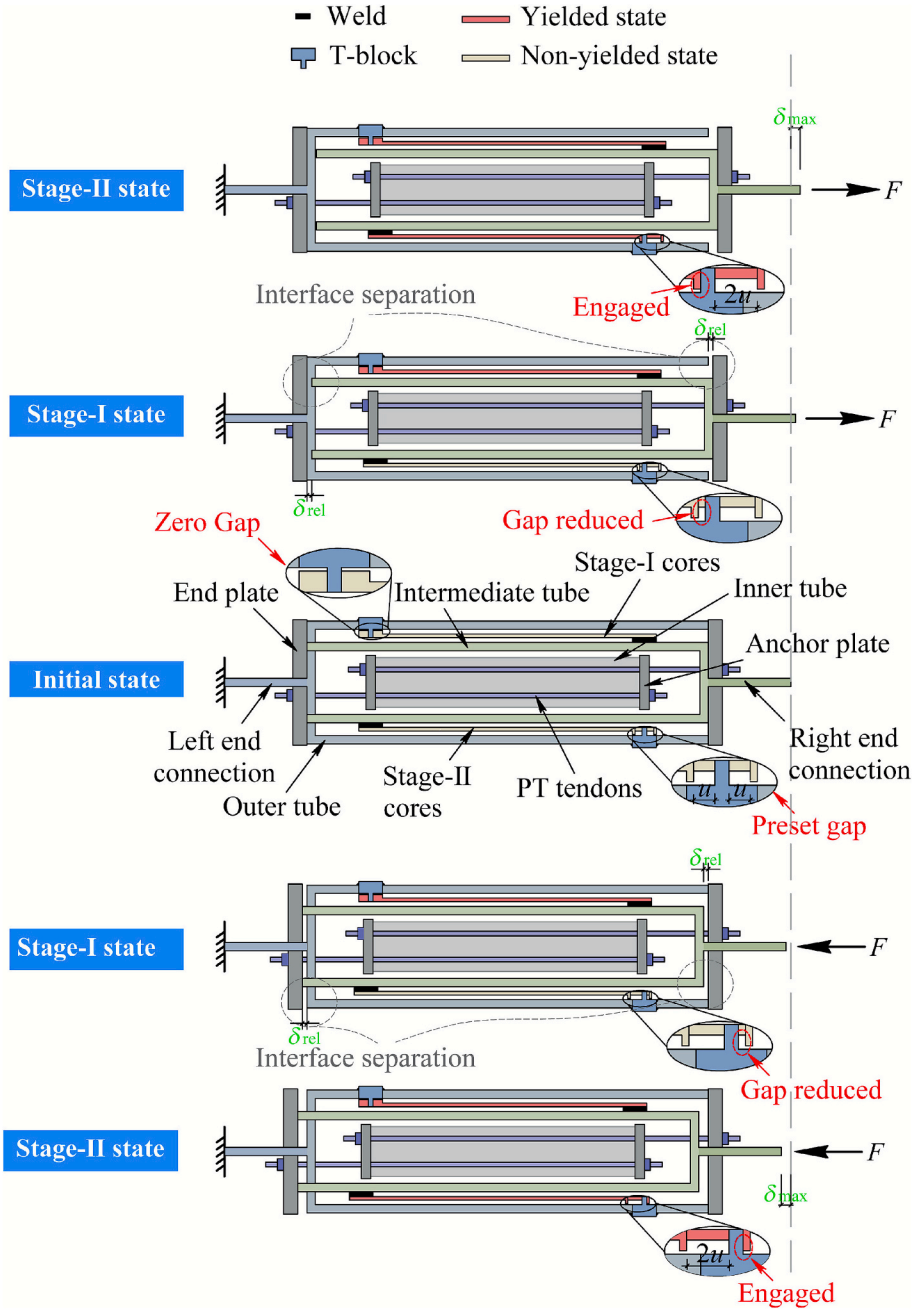

Fig. 2. Working mechanism of the TSCDY-BRB.

2, the SCS is modeled as bilinear elastic with stiffnesses K_{sc1} (pre-activation) and K_{sc2} (post-activation). The initial slope K_{sc1} includes the elastic contribution of the intermediate and outer tubes together with the tendons; after activation, the effective slope reduces to the tendon-only stiffness K_{sc2}. EDS-1 is modeled as bilinear elastoplastic element without gap. EDS-2 is modeled as a gapped bilinear elastoplastic subsystem with a symmetric clearance u at the T-block–hole interface: it remains idle until the local slip reaches u, and upon unloading requires an additional slip of $2u$ to re-engage on the opposite wall.

The activation and peak displacements are δ_a and δ_{max}. The yield displacements of the two groups are δ_{y1} and δ_{y2}, with elastic tangents K_{e1}, K_{e2} and post-yield tangents K_{p1}, K_{p2}. The end-connection stiffnesses are K_{c1} and K_{c2}. The initial tendon prestress is F_p. Component elastic stiffnesses are evaluated as $K = EA/L$ over the effective gauge length.

With the main body and the end connections acting in series, the assembly-end tangent stiffness in any working segment is

$$K_{tot} = \left(\frac{1}{K_{c1}} + \frac{1}{K_{body}} + \frac{1}{K_{c2}}\right)^{-1} \tag{1}$$

where the segment-wise main-body tangent K_{body} is specified in Table 1 according to engagement and yielding states; In the initial stage (segment oa), no sliding occurs and all parts deform together, $K_{body,\,oa} = K_{sc1} + K_{e1}$, hence the assembly initial stiffness and the activation displacement read

$$K_{init} = K_{tot,oa} = \left(\frac{1}{K_{c1}} + \frac{1}{K_{body,oa}} + \frac{1}{K_{c2}}\right)^{-1} \tag{2}$$

$$\delta_a = \frac{F_p}{K_{init}} \tag{3}$$

The SCS has the following two levels of stiffness before and after

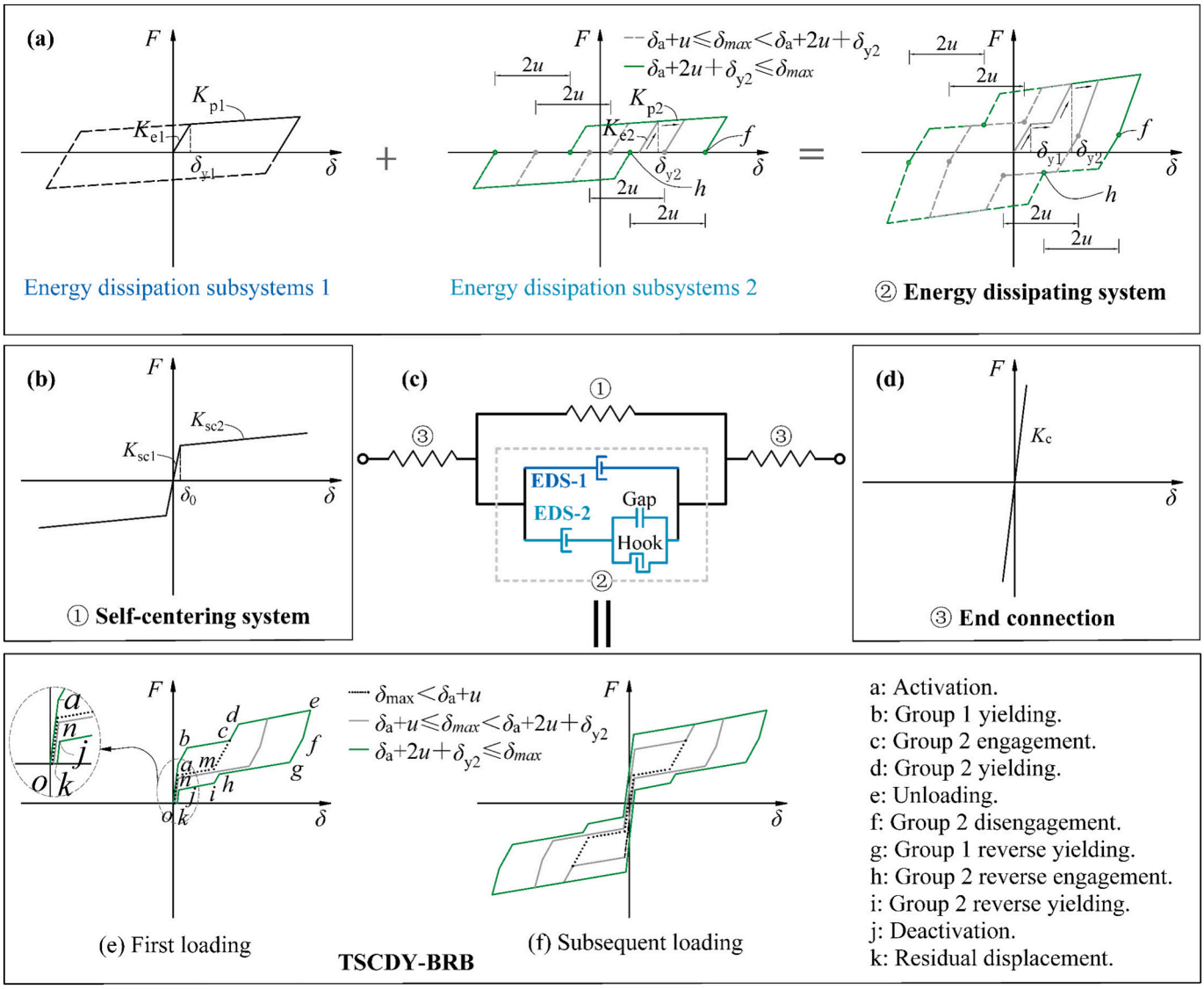

Fig. 3. Simplified physical model and hysteretic behavior of the TSCDY-BRB.

Table 1
Segment-wise tangents and key-point coordinates.

Path	Key-point coordinate	K_{body}
Loading		
o → a	$\delta_a = F_p / K_{init}$ (Eq. (3))	$K_{sc1} + K_{e1}$
a → b	$\delta_b = \delta_a + \delta_{y1}$	$K_{sc2} + K_{e1}$
b → c	$\delta_c = \delta_a + u$	$K_{sc2} + K_{p1}$
c → d	$\delta_d = \delta_c + \delta_{y2}$	$K_{sc2} + K_{p1} + K_{e2}$
d → e	$\delta_e = \delta_{max}$	$K_{sc2} + K_{p1} + K_{p2}$
Unloading		
e → f	δ_f from Eq. (15)	$K_{sc2} + K_{e1} + K_{e2}$
f → g	δ_g from Eq. (16)	$K_{sc2} + K_{e1}$
Case A (re-engage occurs, $\delta_{max} \geq \delta_a + 2u + \delta_{y2}$)		
g → h	δ_H from Eq. (17)	$K_{sc2} + K_{p1}$
h → i	δ_i from Eq. (18)	$K_{sc2} + K_{p1} + K_{e2}$
i → j	$\delta_j = \delta_a$	$K_{sc2} + K_{p1} + K_{p2}$
j → k	δ_k from (Eq. (19))	$K_{sc1} + K_{p1} + K_{p2}$
Case B (no re-engage, $\delta_a + u < \delta_{max} \leq \delta_a + 2u + \delta_{y2}$)		
g → n	$\delta_n = \delta_a$	$K_{sc2} + K_{p1}$
n → k	δ_k from (Eq. (19))	$K_{sc1} + K_{p1}$

Notes. (i) All listed stiffnesses are main body segment tangents K_{body}. the assembly-end tangent used in Eq. (1). (ii) At points j or n, end gaps close; equivalently, the total-displacement coordinate returns to the activation value, i.e., $\delta = \delta_a$.

activation:

$$K_{sc1} = K_{int} + K_{ou} + K_{sd} \tag{4}$$

$$K_{sc2} = K_{sd} \tag{5}$$

where K_{int} and K_{ou} are the axial stiffnesses of the intermediate and outer tubes, and the series equivalent of the tendon sets and inner tube is

$$K_{sd} = \left(\frac{1}{K_{s1}} + \frac{1}{K_{s2}} + \frac{1}{K_{in}}\right)^{-1} \tag{6}$$

where K_{s1}, K_{s2} and K_{in} are the stiffness of the two tendon sets and the inner tube, respectively; for a tendon set with n parallel strands, $K_s = nE_sA_s/L_s$.

For each core plate group $i = 1, 2$, the elastic and post-yield tangents are

$$K_{ei} = \left(\frac{1}{K_{con,i}} + \frac{1}{K_{tr,i}} + \frac{1}{K_{y,i}} + \frac{1}{K_{f,i}}\right)^{-1} \tag{7}$$

$$K_{pi} = \alpha K_{ei} \tag{8}$$

where $K_{con,i}$, $K_{tr,i}$, $K_{y,i}$ and $K_{f,i}$ represent the stiffness of the connection

segments, transition segments, energy dissipation segments and free segments of a given group of core plates; α is the second stiffness ratio, and in this paper, it is set to 0.01.

From the displacement-compatibility condition for a series assembly, the increments of the total device displacement $\Delta\delta$ and the main-body relative slip $\Delta\delta_{rel}$ satisfy

$$\Delta\delta = \left(1 + \beta K_{body}\right)\Delta\delta_{rel} \tag{9}$$

where $\beta = 1/K_{c1} + 1/K_{c2}$. After activation, the end connections are much stiffer than the main body in the configured range ($\beta K_{body} \ll 1$), so $\Delta\delta \approx \Delta\delta_{rel}$. Consequently, the model is evaluated in the total-displacement coordinate, while the mechanism (engagement, elastic recovery, yielding) remains governed by the main-body slip.

3.2. One-cycle loading–unloading path

Fig. 3(e) and (f) illustrate the hysteretic response under initial and cyclic loading. Despite minor differences, the same restoring-force formulation applies; the compression-first case is analogous. Under tension, the brace follows the assembly-end stiffness to the activation displacement at point a, where end gaps open at the tube–end-plate interfaces on both sides as the intermediate and outer tubes slip relative to each other. Stage I then develops with the self-centering system acting in parallel with EDS-1: the Group-1 cores remain elastic to point b, yield at b, and continue with the post-yield tangent to point c. The Group-2 cores are disengaged in this stage, and their first engagement occurs at point c, where $\delta_c = \delta_a + u$. Stage II follows from point c to point e: the Group-2 cores are elastic to point d, yield at d, and loading proceeds to the peak point e with the SCS, EDS-1 and EDS-2 acting together, forming the double-stage skeleton.

Upon reversal from e, all active elements unload elastically. Because EDS-2 carried load on the preceding branch, the Group-2 cores unload and separate at point f and remain idle to point g, where the Group-1 cores reverse-yield. The subsequent path depends on the displacement demand. If $\delta_{max} \geq \delta_a + 2u + \delta_{y2}$ (Case A), the Group-2 cores re-engage after an additional local slip of about 2u at point h, reverse-yield at point i, the path then reaches point j at end-gap closure (simultaneous seating of the end plates against the ends of the intermediate and outer tubes), and tendon recentering returns the response to the zero-force point k; the unloading branch thus also exhibits double-stage yielding. If $\delta_a + u < \delta_{max} \leq \delta_a + 2u + \delta_{y2}$ (Case B), the accumulated local slip from point f to the zero crossing is less than 2u, so no re-engagement occurs; the path proceeds to point n (the simultaneous-seating counterpart of point j) and then to k. If $\delta_{max} < \delta_a + u$, Stage II never activates and the loop reduces to a single-flag response governed by SCS in parallel with EDS-1. Segment-wise tangent stiffness and key-point coordinates are listed in Table 1 and map one-to-one to the labeled segments in Fig. 3(e).

3.3. Restoring-force evaluation and key-point calculations

Building on the stage-wise mechanics summarized in Section 3.2, the response is cast below into a computable piecewise form. Only the segment slope and the state at the starting key point are required to march along the curve.

(a) General line-segment rule

For any segment with constant tangent stiffness $K_{tot,xy}$ (as specified in Eq. (1) and Table 1) and starting key point (δ_x, $F(\delta_x)$), the restoring force within that segment is

$$F(\delta) = F(\delta_x) + K_{tot,xy}(\delta - \delta_x), \quad \delta \in \left[\delta_x, \delta_y\right] \tag{10}$$

(b) Peak-force sharing at e

Let δ_e be the peak displacement. The total restoring force decomposes as

$$F_e = F_p + R_{SCS,e} + R_{1e} + R_{2e} \tag{11}$$

Post-activation, the SCS contributes

$$R_{SCS,e} = K_{sc2}(\delta_e - \delta_a) \tag{12}$$

The force portions carried by EDS-1 and EDS-2 at the peak,

$$R_1(\delta) = \begin{cases} K_{e1}(\delta - \delta_a) & \delta_a \leq \delta \leq \delta_b \\ K_{e1}\delta_{y1} + K_{p1}(\delta - \delta_b) & \delta > \delta_b \end{cases} \tag{13}$$

$$R_2(\delta) = \begin{cases} 0 & \delta \leq \delta_c \\ K_{e2}(\delta - \delta_c) & \delta_c < \delta \leq \delta_d \\ K_{e2}\delta_{y2} + K_{p2}(\delta - \delta_d) & \delta > \delta_d \end{cases} \tag{14}$$

here $\delta_b = \delta_a + \delta_{y1}$, $\delta_c = \delta_a + u$, and $\delta_d = \delta_c + \delta_{y2}$ (Table 1), so $R_{1e} = R_1(\delta_e)$, $R_{2e} = R_2(\delta_e)$.

(c) Coordinates of key points on the unloading branch

Starting from e, the coordinates of the unloading key points follow from elastic recovery of the engaged elements and the fixed $2u$ re-engagement at the T-block–hole interface:

First disengagement of Group-2 (point f):

$$\delta_f = \delta_e - \frac{R_{2e}}{K_{e2}} \tag{15}$$

Reverse yielding of Group-1 (point g):

$$\delta_g = \delta_e - \left(\frac{R_{1e}}{K_{e1}} + \delta_{y1}\right) \tag{16}$$

For Case A re-engagement and reverse yielding of Group-2 (points h, i)

$$\delta_h = \delta_f - 2u \tag{17}$$

$$\delta_i = \delta_h - \delta_{y2} \tag{18}$$

For Case B, no re-engagement occurs before the zero crossing and points h and i are absent.

For the last segment x–k (x = j or n) that contains the zero crossing, the residual displacement is

$$\delta_k = \delta_x - \frac{F(\delta_x)}{K_{tot,xk}} \tag{19}$$

where $K_{tot,xk}$ is the assembly-end tangent over x–k from Eq. (1) and Table 1.

The above peak-sharing definitions $R_{scs,e}$, R_{1e}, R_{2e} close the expressions for the unloading key points (δ_f, δ_g, δ_h, δ_i). Combined with the segment stiffness entries in Table 1 and the general line rule, they provide a self-contained and reproducible evaluation of the restoring force over the entire loop. For simplicity, isotropic and kinematic hardening of the core steel are not included in the closed-form model; they will be considered in the numerical study to better reflect possible field behavior.

4. Numerical simulation

4.1. Specimen geometry and dimensions

This subsection briefly summarizes the quasi-static test program only to give context for the finite element (FE) and test comparison; the full experimental procedures and observations are documented separately and are not detailed here, the present study focused on the modelling approach, mechanism verification, and parametric analysis. The

numerical model uses the nominal dimensions of the full-scale TSCDY-BRB specimen. The overall geometry and key sizes are shown in Fig. 4. It is noted that the relatively large brace-end widths shown in Fig. 4 were chosen to suit the spacing and clearance of the laboratory reaction frame and actuator grips, and can be reduced in building applications without affecting the proposed self-centering double-stage mechanism or the restoring-force model.

The two groups of core plates and the restraining plates are 8 mm thick, and the buckling-restraining plates are 10 mm thick. The core plates are Q235 steel; all other steel parts are Q345. The self-centering system uses 4 prestressed steel strands with a diameter of 15.2 mm. The total prestress is set as $F_p = \varphi F_{y,tot} = 141$ kN, where $\varphi = 1.5$ and $F_{y,tot}$ is the total yield force of the two groups of core plates. The T-block fits the rectangular openings of the Group-1 cores with zero clearance, while a lateral gap of $u = 5$ mm between the two sidewalls of the Group-2 cores openings. Fig. 5 shows the test setup (PWS-4000 loading system, 4000 kN static capacity). The specimen, which serves as the first full-scale validation test of the TSCDY-BRB concept, was installed horizontally between the reaction block and the actuator with pin connections at both ends. Displacement-controlled loading was applied with peak amplitudes of 2, 4, 6, 8, 10, 12, 14, 16 and 18 mm. With these dimensions and prestress, an end displacement of 18 mm corresponds to an additional elongation of about 9 mm in each tendon set ($\approx$ 0.4% strain), so that the peak tendon strain, including the initial prestress ($\approx$ 0.25%), is about 0.65%, which is below the design elastic limit (0.75%) and the measured yield strain of the strands. Within this range the hysteretic loops remained stable and repeatable, showing a flag-shaped response; as the displacement increased, the second group of core plates gradually engaged and the loops evolved into the intended double-stage pattern, without noticeable strength or stiffness degradation or visible global bowing of the brace. The measured monotonic stress–strain curves of the strand, Q235 and Q345 steels are shown in Fig. 5(b), and the corresponding test results are listed in Table 2. These results are used to define the material models in the FE analysis.

4.2. Finite element modelling

A three-dimensional FE model of the TSCDY-BRB was developed in Abaqus. Prestressing strands were modeled with T3D2 truss elements, and all other parts with eight-node linear reduced-integration solids (C3D8R). To capture cyclic hardening and the Bauschinger effect of the core plates under load reversals, a combined isotropic–kinematic hardening law was adopted. The parameters of this mixed hardening model were taken with reference to [42] and then calibrated by matching simulations to the test results. For the remaining components that primarily provide restraint or load transfer, material properties were obtained from material tests and represented by a bilinear kinematic model. Considering that there are many contacts in the assembly, we introduce simple modelling choices to keep the analysis stable and efficient without losing accuracy. Considering the numerous contact interfaces in the assembly, simple modelling choices were adopted to keep the analysis robust and efficient without sacrificing accuracy at the global-response level. Bolts at both end connections were not modeled explicitly, as they primarily serve to assemble the parts and would introduce many small, irregular contact pairs; welded and bolted interfaces were instead represented by Tie constraints. In the physical test, lithium-based grease was applied to the yielding segments of the core plates to reduce friction against the restraining members. Because explicit contact modelling tends to cause numerical instability and convergence difficulties and is extremely time-consuming, several effective simplifications for the restraining units have been reported in the literature [43]. Guided by repeated simulation–test comparisons, the restraining units were represented as boundary restraints that capture the out-of-plane constraint on the core. For the interfaces between the end plates and the tubes, and between the T-shaped block and the rectangular openings of the core plates, the normal behavior is defined as hard contact with separation allowed after contact; the tangential behavior uses penalty-formulation Coulomb friction with a friction coefficient of 0.1. Strand anchorage to the end plates is realized by kinematic coupling between the strand end nodes and the anchoring surfaces. Prestress F_p is applied using the temperature method (cooling) before cyclic loading. Boundary conditions and the displacement-controlled loading history match the test: the left end connected to the outer tube is fixed; the outer surface of the right end, which is connected to the middle tube, is coupled to a reference point (RP-1), and the cyclic displacement is prescribed at that point. The mesh is refined where plasticity and contact occur, 10 mm in the yielding parts of the T-block and the core plates, and 20 to 50 mm elsewhere. The full FE model is shown in Fig. 6.

4.3. Model validation

To validate the finite element model, simulated hysteresis loops were compared with quasi-static tests at three displacement amplitudes (Fig. 7). For each amplitude, the average peak loads in tension and compression and the single-cycle energy dissipation E_D (area enclosed by the hysteresis loop) were extracted and compared with the tests (Table 3), with relative errors within 15% In addition, the model reproduces the segmental tangents and the characteristic strengths within the same accuracy range. The simulations also capture re-engagement after an additional slip of about $2u$ and the shift of the second yield point to the unloading branch, consistent with the theoretical mechanism. Although a few individual errors exceed this range and the tests exhibit larger residual displacements than both the simulations and the theoretical predictions, the modelling strategy and material inputs capture the main features of the brace hysteresis. The remaining discrepancies likely arise from incomplete and time-dependent prestress, fabrication tolerances and geometric imperfections, limited slip at bolted or pinned connections, and modelling idealizations such as omitting explicit bolt representation and using simplified contact.

Fig. 7 (b) reveals the two working stages of the brace predicted in Sections 2–3. In stage AC, only the first-stage core yields. In stage BE, both the first- and second-stage cores yield, and the load capacity increases. During loading, the end gap between the outer end plate and the tubes equals the sum of strand elongations. When the two strand groups have the same length, the elongation of one group is approximately half of the end gap. Fig. 7(c) shows that, in the FE results, the strand elongation is about half of the predicted end-gap opening at the tube–end-plate interfaces, which is consistent with the intended tandem tendon mechanism [11].

Fig. 8 shows the von Mises stress contours at the maximum imposed displacement of 18 mm. In the FE results, plastic strains concentrate in the reduced yielding segments of the two core-plate groups, while the tubes, T-shaped block and end plates remain essentially elastic, indicating that the dominant inelastic mechanism in the present test range is stable yielding of the core plates rather than buckling-induced degradation. Interface separation (end-gap opening) is observed at the tube–end-plate interfaces on both sides under tension and compression. The two core-plate groups engage sequentially and yield in their designated zones, while the remaining members stay elastic. The prestressing strands experience the largest computed stresses among the modeled components but do not reach yield under the specified material properties. Local stress concentrations occur near the anchorages of the inner and outer end plates. These results are consistent with the proposed mechanism and the simulated hysteresis and support the fidelity of the finite-element model. It should be noted that the end-gap opening was not directly instrumented in the physical test; its evolution is inferred from the calibrated FE model and the restoring-force model. Future TSCDY-BRB tests will adopt a bolted, demountable configuration so that the end gaps and internal sliding gaps can be measured directly.

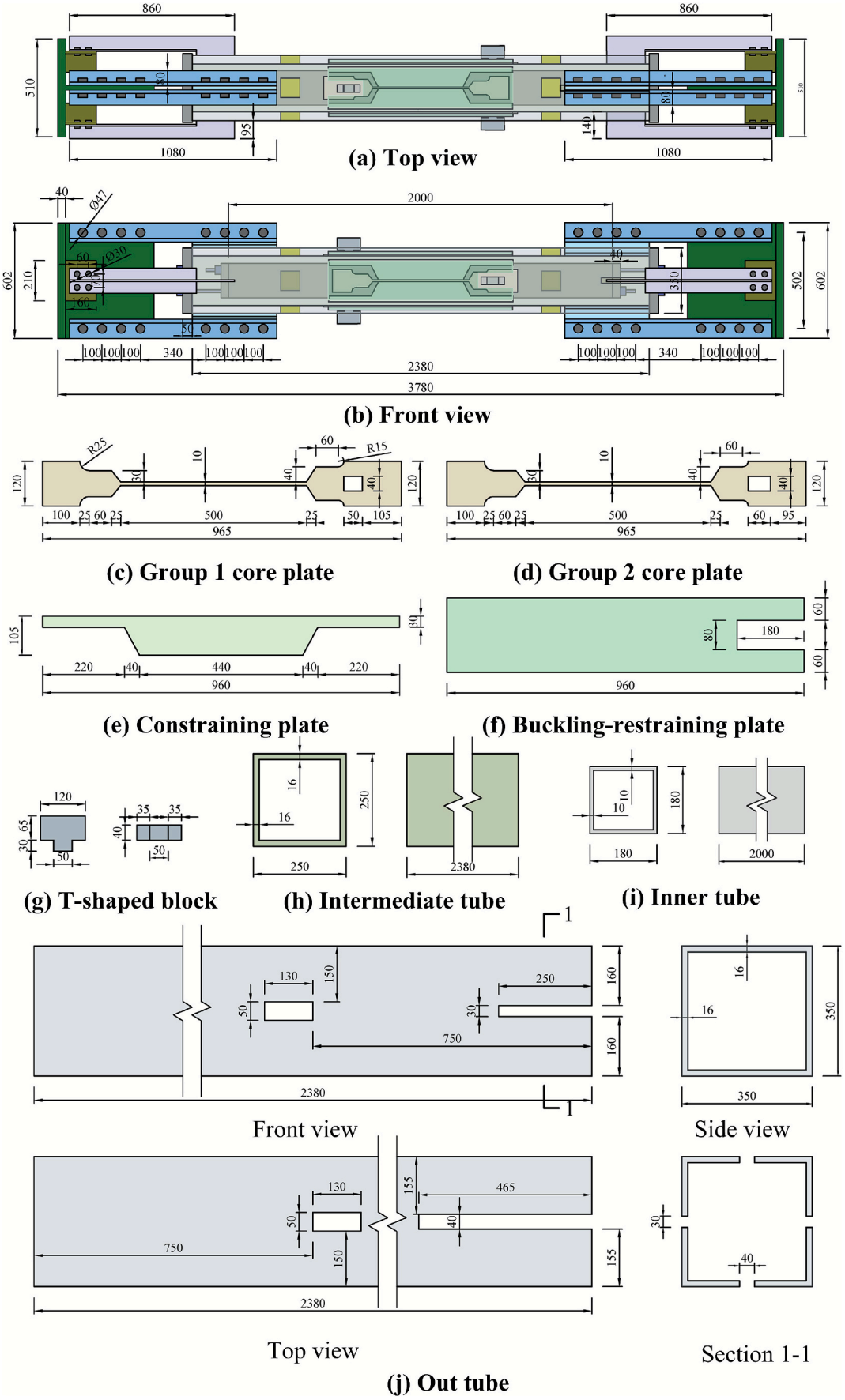

Fig. 4. Dimensions of the TSCDY-BRB (units: mm).

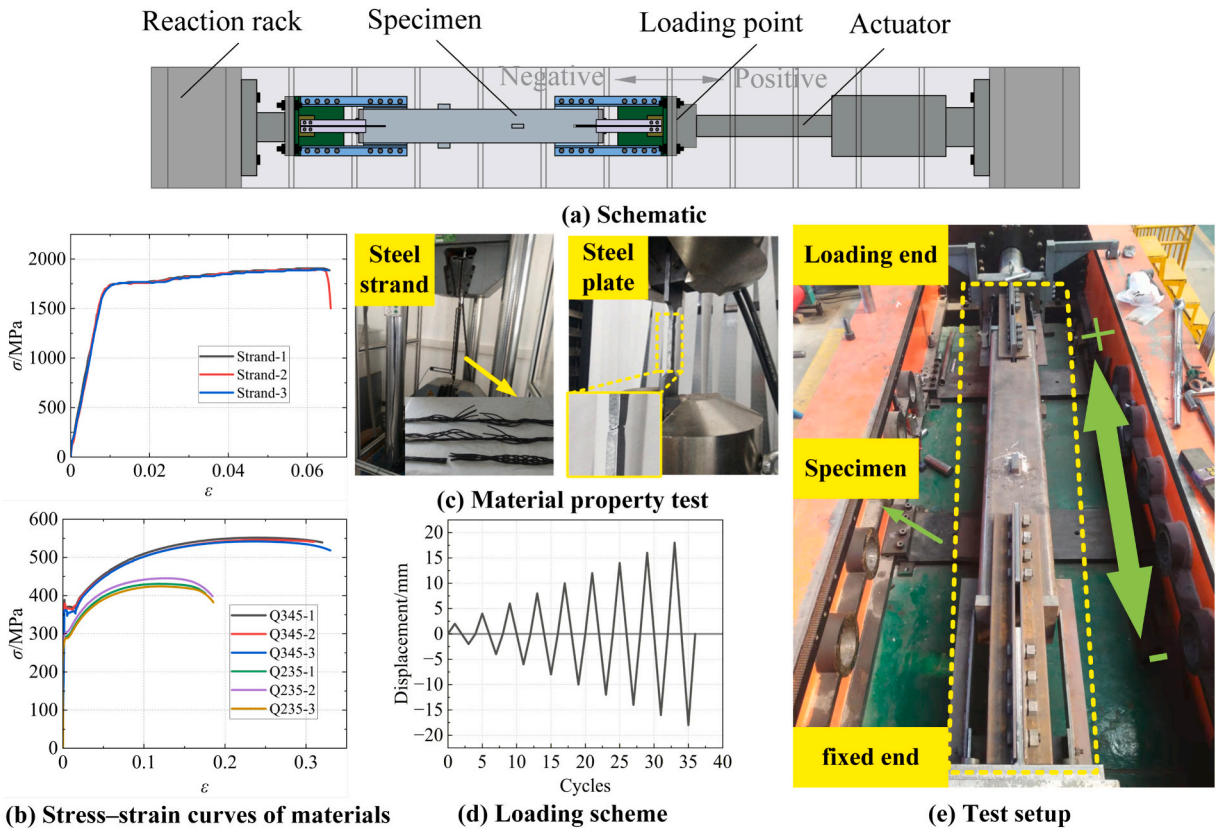

Fig. 5. The schematic diagram of the quasi-static test of TSCDY-BRB.

Table 2
Material properties.

Material	f_y/MPa	f_u/MPa	E/GPa
Strand	1745.3	1901	201
Q235	294.2	432.2	206
Q345	372.8	546.1	206

Note: f_y, f_u, and E are the yield strength, nominal maximum stress, and Young's modulus, respectively.

5. Parametric analysis

Following the validation in section 4, this section presents a parametric numerical study to quantify the influence of five design variables: the prestress (P), strand diameter (D), cross-sectional areas of the Group-1 and Group-2 cores yielding segments (A_1 and A_2), and the preset gap (U) on the TSCDY-BRB hysteretic response. The previously defined analysis model 1 is used as the reference, around which 16 one-factor variants are constructed (Table 4). The response metrics include the characteristic forces F_A and F_B at the stiffness change points of the subsequent loading curve and the segmental tangential stiffnesses K_{OA}, K_{AC}, K_{CD}, K_{BE} of the labeled segments [8] (Fig. 7 (b)), for which the corresponding values for model 1 are 185.79 kN, 261.34 kN, 566.20 kN/mm, 13.05 kN/mm, 55.75 kN/mm, and 14.19 kN/mm. Table 4 records each quantity in dimensionless form as the ratio to Model 1. Overall performance is additionally assessed by the equivalent viscous damping ratio ξ_{eq} ($\xi_{eq} = E_D/(2\pi K\Delta^2)$), computed from the single-cycle energy dissipation E_D, the secant stiffness K, and the peak displacement Δ) and the residual displacement δ_r.

5.1. Effect of prestress P

Fig. 9 shows that all four hysteresis loops retain a full flag shape for all prestress levels. As P increases, the traces in the first and fourth quadrants shift upward, while the segmental tangent stiffnesses remain nearly unchanged. From Table 4, relative to Model 1, F_A ranges from 0.66 to 1.15 of the baseline and F_B from 0.74 to 1.12, while K_{OA}, K_{AC}, K_{CD}, and K_{BE} remain at the baseline. This indicates that prestress lifts the force baseline and the characteristic strengths, while the stiffnesses are governed mainly by geometry and material property and are only weakly related to P.

Fig. 10 further shows that E_D is essentially insensitive to P, at the 18 mm amplitude the spread among the curves is below about 3%. ξ_{eq} decreases from 0.148 to 0.118 as P increases, a reduction of about 21%. This is because, at the same peak displacement, higher prestress raises the elastic force level and the effective stiffness, so more of the input is stored elastically while the plastic work changes little. A short dip over a narrow amplitude range is more noticeable at lower prestress when the Group-2 cores engage but remain elastic; this added elastic participation briefly lowers ξ_{eq} until yielding develops. δ_r at 18 mm decreases markedly with prestress, from about 3.35 mm to about 0.40 mm, showing stronger self-centering.

5.2. Effect of strand diameter D

Fig. 11 shows that enlarging D makes the subsequent loading and unloading-return branches steeper, while the loops remain full and the initial loading segment changes little. Relative to Model 1, F_A stays within 0.99–1.03 of the baseline, F_B and K_{OA} varies within 4%. In contrast, the later-stage tangent stiffnesses after activation are highly sensitive to diameter, K_{AC} ranges from 0.73 to 1.87 of the baseline, K_{BE} from 0.75 to 1.82, and K_{CD} from 0.93 to 1.24. Thus, strand diameter mainly tunes the stiffness of the later-stage branches rather than the initial strength.

Fig. 12 shows that E_D grows with displacement and is only weakly affected by diameter. At 18 mm it decreases slightly from about 6.88 to

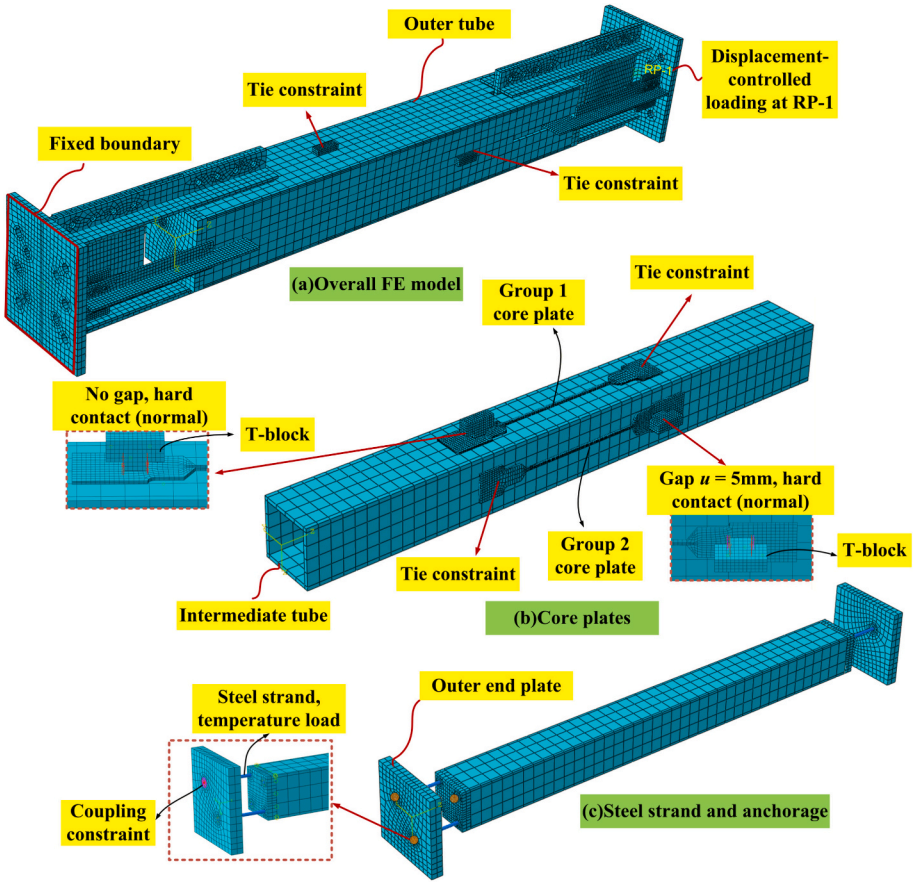

Fig. 6. FE model of the TSCDY-BRB.

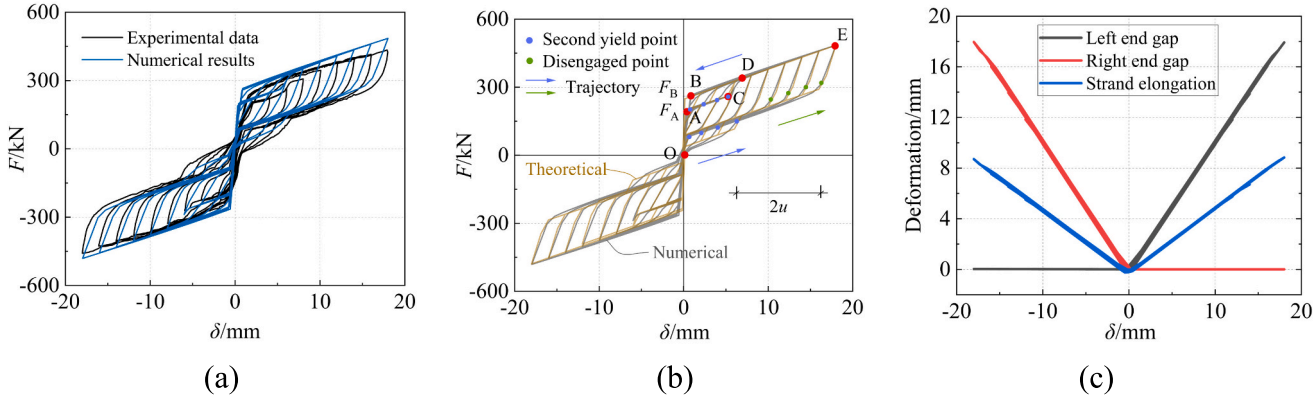

Fig. 7. Validation of the FE model: (a) hysteresis comparison; (b) double-stage response; (c) tandem self-centering mechanism.

Table 3
Comparisons of the test results and estimated values.

Amplitude /mm	Peak load average value/kN			Energy dissipation/kJ		
	Experiment	Theory	Simulation	Experiment	Theory	Simulation
4	222.75	245.05 (10.00)	242.19 (8.73)	0.52	0.67 (28.85)	0.56 (7.69)
10	351.44	376.65 (7.14)	378.94 (7.82)	2.68	2.69 (0.37)	2.55 (4.85)
18	446.52	481.87 (7.92)	483.23 (8.22)	6.93	6.26 (9.67)	6.75 (2.60)

6.53 kJ as diameter increases. ξ_{eq} also decreases with diameter, at 18 mm it falls from 0.142 to 0.087, a reduction of about 39%. The reason is

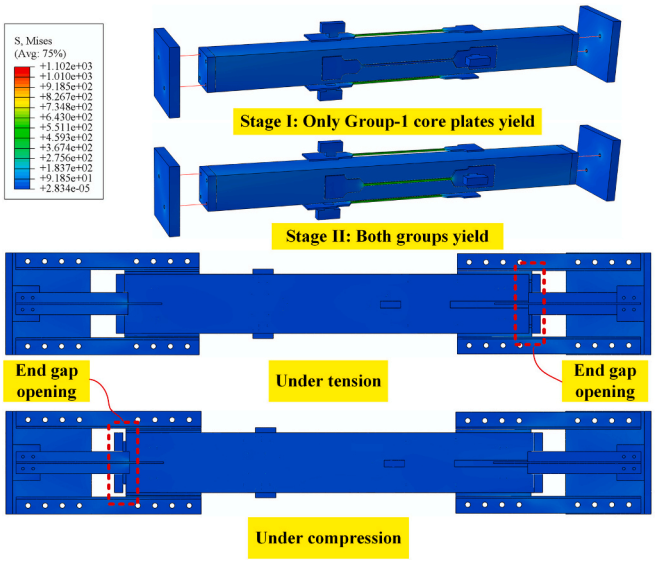

Fig. 8. Stress contour of specimen (units: MPa).

that stiffer strands carry more load elastically at the same peak displacement, so more energy is stored and returned elastically and less is dissipated plastically. δ_r decreases slightly with diameter and remains small overall, with a maximum of only about 0.54 mm.

5.3. Effect of Group-1 core area A_1

Fig. 13 shows that larger A_1 makes the loops progressively fuller. The Stage I strength and the initial slope rise clearly, while the subsequent branches change little. Relative to Model 1, F_A is about 1.10–1.28 of the baseline, F_B about 1.05–1.25, and K_{OA} about 1.10–1.28; K_{AC}, K_{CD} and K_{BE} increase only slightly, generally within about 10%. These results confirm that the Group-1 cores govern the onset of yielding and the overall initial stiffness; hence the largest gains appear in F_A and K_{OA}, with F_B also increasing because the Stage II capacity includes the Group-1 contribution.

Fig. 14 show that E_D increases over the whole displacement range; at 18 mm it rises from about 6.75 to 10.5 kJ, an increase of about 56%. ξ_{eq} also increases and at 18 mm rises from about 0.124 to 0.171, about 38% higher, because a larger A_1 engages more Stage I plasticity and the plastic share becomes larger. δ_r increases notably with A_1; at 18 mm it grows from about 0.51 to 3.15 mm, roughly a sixfold rise, indicating that heavier Stage I plastic deformation weakens self-centering.

5.4. Effect of Group-2 core area A_2

Fig. 15 shows that larger A_2 raises and stiffens the Stage II branch, while the Stage I branch changes little. Compared with A_1, the enhancement in loop fullness is less pronounced. From Table 4, F_A, K_{OA} and K_{AC} stay at the baseline; F_B increases to about1.02–1.21, K_{CD} to about 1.14–1.51, and K_{BE} to about 1.01–1.04, with K_{CD} showing the largest gain of 51%.

Fig. 16 show that E_D increases with A_2, at 18 mm it increases from about 6.75 to 9.01 kJ; ξ_{eq} increases modestly with A_2, at 18 mm it rises from about 0.124 to 0.147, with a brief mid-amplitude inversion because the Group-2 cores first engage mainly elastically and add elastic input before yielding develops; δ_r increases from about 0.51 to 1.97 mm, about four times. Overall, A_2 mainly governs Stage II strength and stiffness and contributes to high-amplitude energy dissipation once

Table 4
Parametric models and response metrics.

Specimen ID	Design variables					Response metrics					
	A_1/mm^2	A_2/mm^2	P/kN	D/mm	U/mm	F_A	F_B	K_{OA}	K_{AC}	K_{CD}	K_{BE}
1	80	80	141	15.2	5	1.00	1.00	1.00	1.00	1.00	1.00
2	80	80	71	15.2	5	0.66	0.74	1.00	1.00	1.00	1.00
3	80	80	101	15.2	5	0.81	0.86	1.00	1.00	1.00	1.00
4	80	80	171	15.2	5	1.15	1.12	1.00	1.00	1.00	1.00
5	80	80	141	12.7	5	0.99	1.01	1.01	0.73	0.93	0.75
6	80	80	141	17.8	5	1.01	1.03	1.03	1.32	1.09	1.30
7	80	80	141	21.6	5	1.03	1.04	1.04	1.87	1.24	1.82
8	104	80	141	15.2	5	1.10	1.05	1.10	1.02	1.02	1.03
9	128	80	141	15.2	5	1.19	1.16	1.19	1.04	1.03	1.05
10	152	80	141	15.2	5	1.28	1.25	1.28	1.08	1.06	1.06
11	80	104	141	15.2	5	1.00	1.02	1.00	1.00	1.14	1.01
12	80	128	141	15.2	5	1.00	1.12	1.00	1.00	1.39	1.03
13	80	152	141	15.2	5	1.00	1.21	1.00	1.00	1.51	1.04
14	80	80	141	15.2	3	1.00	1.00	1.00	1.00	1.00	1.00
15	80	80	141	15.2	7	1.00	–	1.00	1.00	1.00	1.00
16	80	80	141	15.2	9	1.00	–	1.00	1.00	1.00	1.00

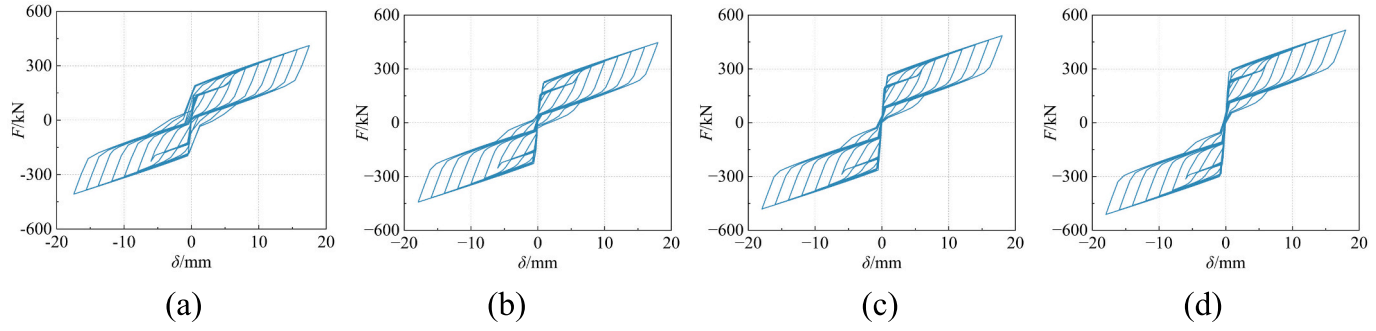

Fig. 9. Hysteretic curves of TSCDY-BRB with different prestress: (a) 71 kN, (b) 101 kN, (c) 141 kN, and (d) 171 kN.

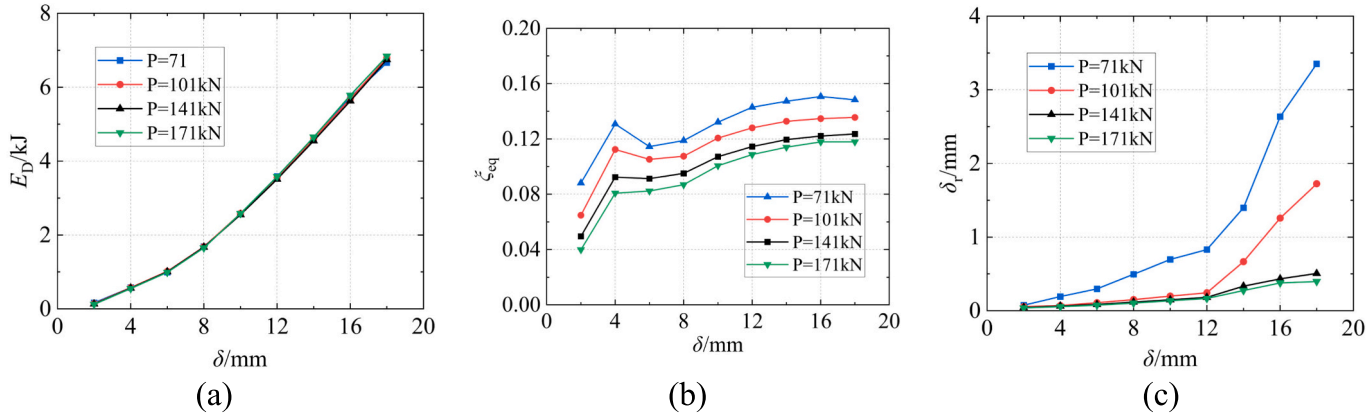

Fig. 10. Comparison of performance indices for analysis models: (a) energy dissipation, (b) equivalent viscous damping ratio, and (c) residual displacement.

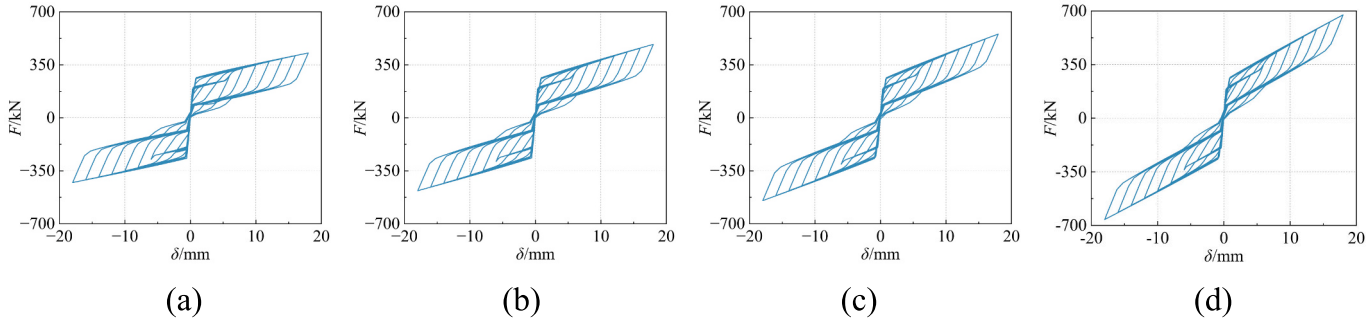

Fig. 11. Hysteretic curves of TSCDY-BRB with different strand diameter: (a) 12.7 mm, (b) 15.6 mm, (c) 17.8 mm, and (d) 21.6 mm.

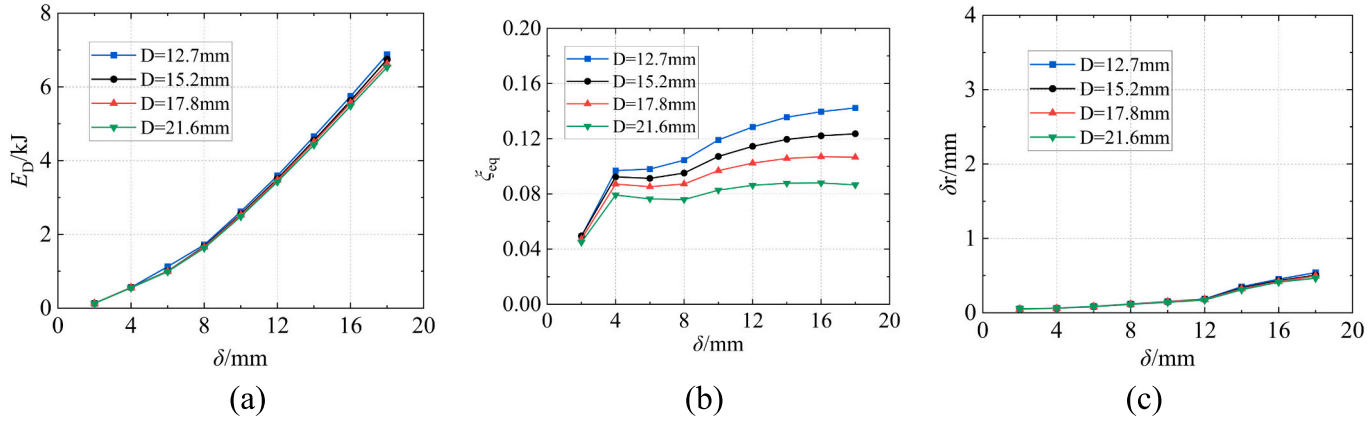

Fig. 12. Comparison of performance indices for analysis models: (a) energy dissipation, (b) equivalent viscous damping ratio, and (c) residual displacement.

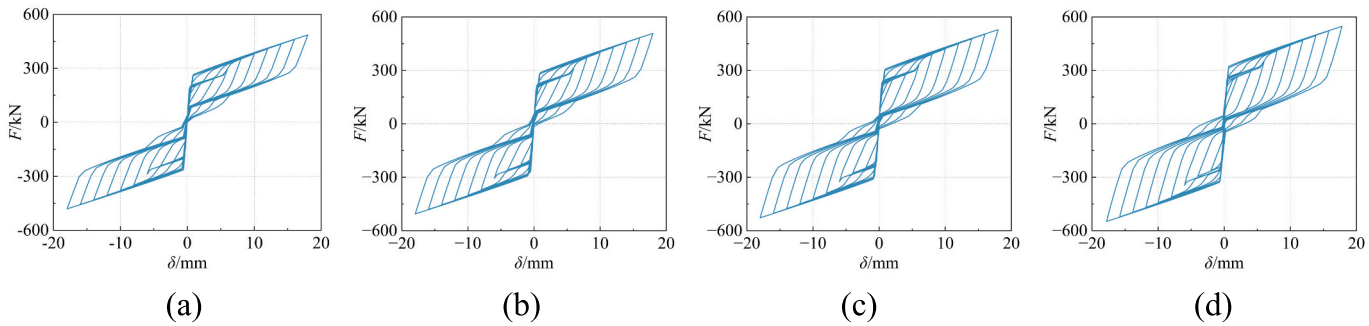

Fig. 13. Hysteretic curves of TSCDY-BRB with different area of A_1: (a) 80 mm^2, (b) 104 mm^2, (c) 128 mm^2, and (d) 152 mm^2.

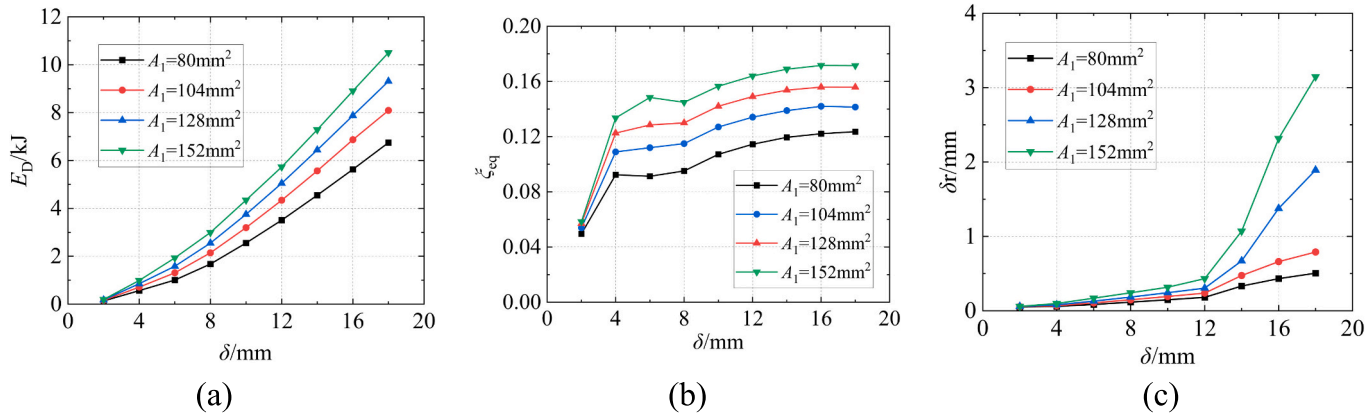

Fig. 14. Comparison of performance indices for analysis models: (a) energy dissipation, (b) equivalent viscous damping ratio, and (c) residual displacement.

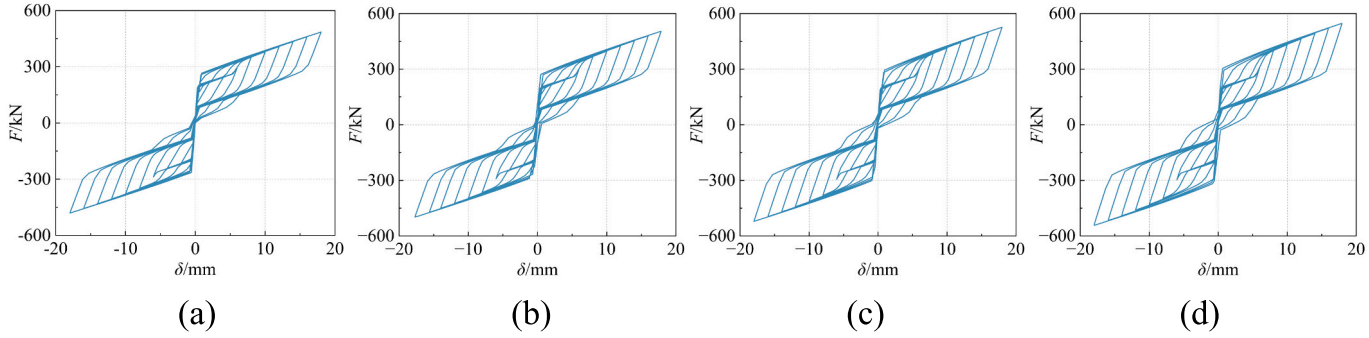

Fig. 15. Hysteretic curves of TSCDY-BRB with different area of A_2: (a) 80 mm^2, (b) 104 mm^2, (c) 128 mm^2, and (d) 152 mm^2.

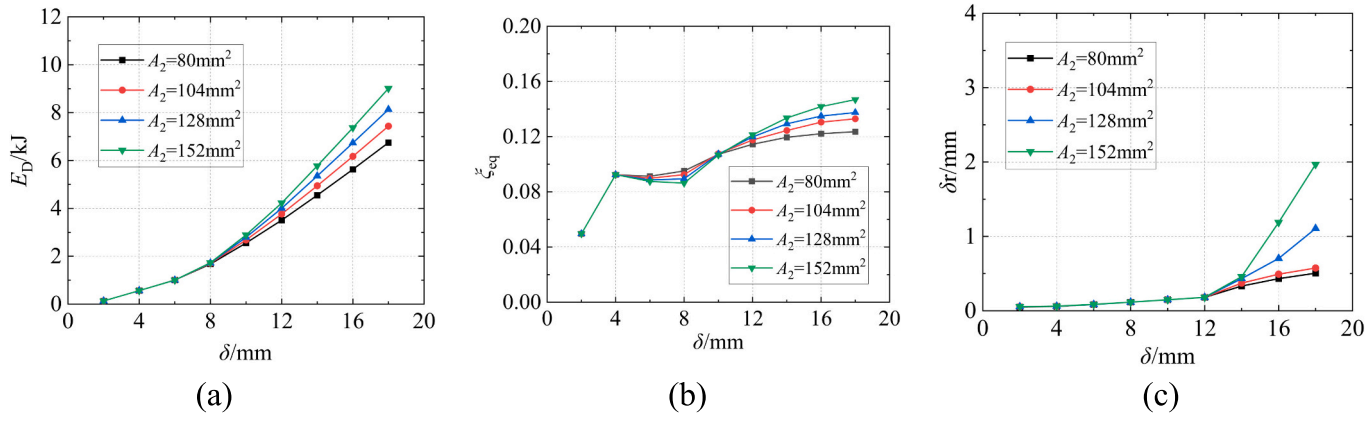

Fig. 16. Comparison of performance indices for analysis models: (a) energy dissipation, (b) equivalent viscous damping ratio, and (c) residual displacement.

engaged.

5.5. *Effect of preset gap U*

Fig. 17 shows that enlarging U delays the engagement of the Group-2 cores and reduces loop fullness. At U of 3 and 5 mm the Group-2 cores engage in both loading and unloading. At U of 7 mm the response is transitional. At U of 9 mm the Group-2 cores engage on loading but not on unloading under the present displacement demand, consistent with Section 2. Table 4 indicates that F_A and the segmental stiffnesses remain at the baseline. For the larger gaps, F_B is not identified because the subsequent loading branch has not yet transitioned to point B. The preceding unloading did not re-engage and yield the Group-2 cores, as the peak drift is below the threshold defined by the activation displacement, twice the preset gap, and the Group-2 yield displacement. In the baseline specimen, U = 5 mm is therefore adopted as a moderate gap that, under the target displacement of 18 mm, produces clear two-stage behavior with Stage II participation on both loading and unloading while keeping the plastic demand of the Group-2 cores at a reasonable level.

Fig. 18 show clear monotonic trends at the target amplitude. E_D decreases with U and at 18 mm drops from about 7.38 to 5.67 kJ, a reduction of about 23%. ξ_{eq} also decreases with U and at 18 mm falls from about 0.135 to 0.104. The crossover and inversion occur because a smaller gap triggers earlier but mostly elastic engagement of the Group-2 cores, increasing elastic input and temporarily lowering ξ_{eq}, Larger

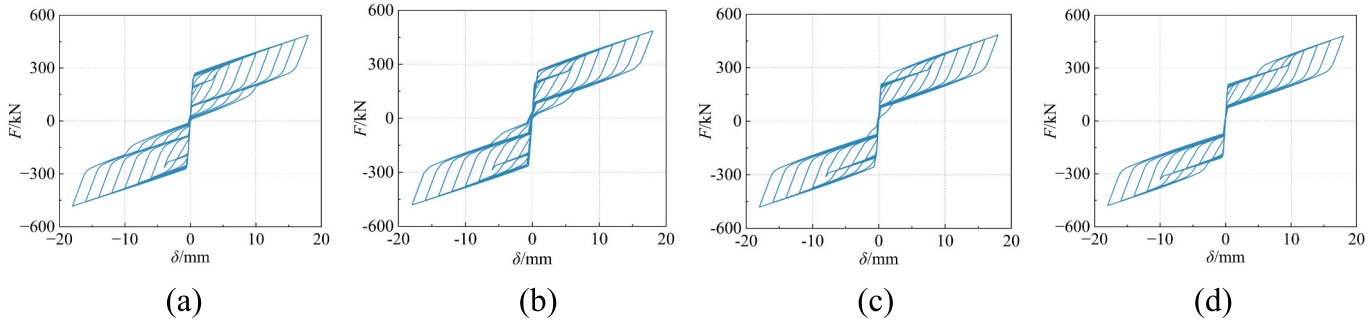

Fig. 17. Hysteretic curves of TSCDY-BRB with different preset gap value of *U*: (a) 3 mm, (b) 5 mm, (c) 7 mm, and (d) 9 mm.

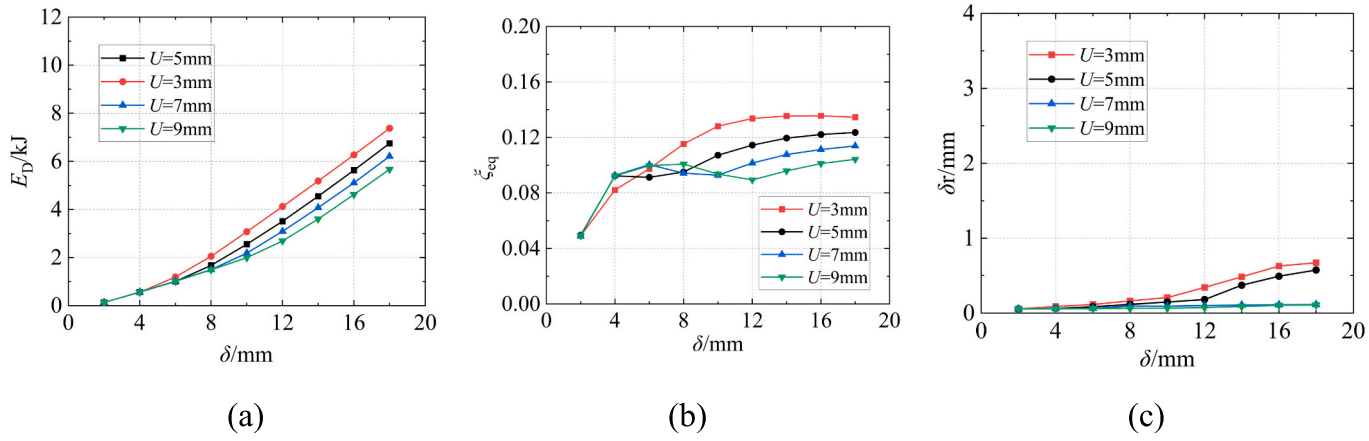

Fig. 18. Comparison of performance indices: (a) energy dissipation, (b) equivalent viscous damping ratio, and (c) residual displacement.

gaps delay this elastic participation and can show a higher ξ_{eq} at that stage; once yielding develops, the case with a smaller gap overtakes due to greater plastic dissipation. δ_r decreases steadily with *U* and at 18 mm reduces from about 0.672 to 0.110 mm. The reason is that a smaller gap triggers Stage II participation earlier and accumulates more plastic deformation in the Group-2 cores, which weakens self-centering, while a larger gap postpones that plastic work and improves recentering.

6. System-level analysis

6.1. Prototype frame and analysis model

Nonlinear response-history analyses were conducted on a six-story planar steel frame to assess the system-level performance of the proposed brace. The frame layout and member sizes follow the prototype reported in Ref. [48], with five 6.6 m bays and a story height of 3.1 m. As shown in Fig. 19, the columns and beams are wide-flange H sections of 700 × 300 × 18 × 34 mm and 400 × 300 × 13 × 21 mm, respectively, both made of Chinese steel Q235. To account for the slab constraint effect on the beams, their Young's modulus was taken as 1.2 times that of the columns, consistent with Ref. [48].

Since the gravity loads were not provided in Ref. [48], an equivalent non-structural mass of 2800 kg was assigned to each floor beam to match the reported first two natural periods of the bare frame, approximately 0.71 s and 0.22 s. After installing the braces described below, the first two periods of the braced frames reduce to 0.31 s and 0.10 s, reflecting the stiff brace configuration.

The tested TSCDY-BRB specimen was used as a reference, with properties adjusted to match the frame's specific geometry. Diagonal braces were installed in the second and fourth bays at each story, following the layout in Ref. [48]. For comparison, a double-stage yielding BRB (DY-BRB) frame was constructed by removing the self-centering branch while preserving the same initial axial stiffness and first stage yield force as the TSCDY-BRB. The combined stiffness and yield force of the SC and BRB_1 branches in the TSCDY-BRB were lumped into a single BRB branch in the DY-BRB, giving a first stage yield force of about 188 kN and initial axial stiffness of 6×10^5 kN/m. The second stage BRB branch (BRB_2) was kept identical in both systems, with the same stiffness, yield force (47 kN) and activation gap ($u = 5$ mm).

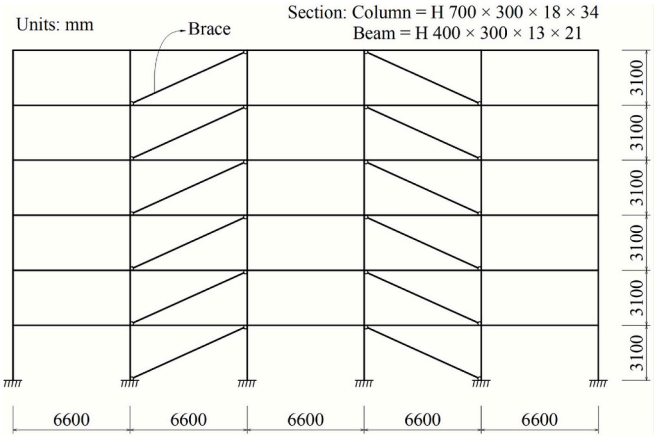

Fig. 19. Prototype steel frame with diagonal braces.

This analysis model represents a "strong-brace, weak-frame" system, designed to concentrate inelastic action in the braces and highlight residual drift control, rather than to propose a complete building design guideline. Beams and columns were modeled with nonlinear beam elements, and rigid diaphragms were enforced at each floor by tying all

joints to a master node. The TSCDY-BRB and DY-BRB components were modeled using axial connector elements calibrated against the tests and the FE simulations in the preceding sections. Rayleigh damping was applied, with the first and second modes of the bare frame having a 4% damping ratio, consistent with Ref. [48]. All analyses were performed using ABAQUS.

6.2. Earthquake records

Three horizontal ground motions (El-Centro, Taft, and a spectrum-compatible artificial record) were selected to represent seismic actions for a region with seismic fortification intensity 8 and Site Class II soil conditions according to the Chinese seismic design code [49]. Two intensity levels were considered: a design-basis earthquake (DBE, PGA = 0.2 g) and a maximum-considered earthquake (MCE, PGA = 0.4 g).

To ensure spectral compatibility, the response spectra of the selected records were first scaled to match the shape of the 5%-damped Chinese design spectrum over the period range 0.2 T_1 to 1.5 T_1, which covers the fundamental and higher-mode responses. Subsequently, this spectrally consistent suite of records was uniformly scaled to achieve the target PGA levels of 0.2 g for the DBE and 0.4 g for the MCE analyses. The same set of processed motions was applied to both the TSCDY-BRB and DY-BRB frames. Fig. 20 compares the 5%-damped spectra of the three scaled records and their mean with the target design spectrum for the 0.2 g level.

6.3. Time history analysis

For system-level evaluation, the peak inter-story drift ratio (IDR) and the residual inter-story drift ratio (RIDR) are critical indicators of seismic performance. Floor responses were obtained from the diaphragm reference nodes, and IDRs and RIDRs were calculated from the relative displacements between adjacent stories. Unless otherwise stated, the results presented are averaged over the three ground motions. Fig. 21 compares the envelopes of the average peak IDR and RIDR for the TSCDY-BRB and DY-BRB frames under the two intensity levels, and additionally presents representative brace hysteresis loops at the third story.

Under the 0.2 g (DBE) motions [Fig. 21(a)], both frames exhibit similar IDR distributions, with the largest drifts occurring in the middle stories and remaining well below the serviceability limit of 1/250. The TSCDY-BRB frame shows a mean IDR of about 0.18%, with a maximum of 0.24%. The corresponding values for the DY-BRB frame are 0.12% and 0.17%. Therefore, despite identical design stiffness and yield force, the TSCDY-BRB frame exhibits peak drifts approximately 1.5 times those of the DY-BRB frame, though both values remain very small.

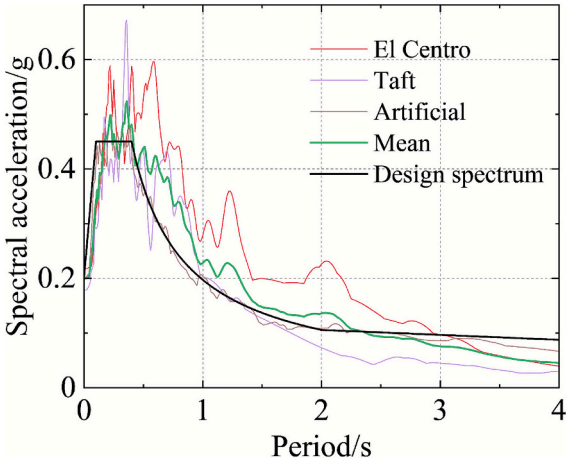

Fig. 20. Acceleration response spectra of the selected ground motions and design spectrum.

Under the 0.4 g (MCE) motions, the second stage cores are more extensively activated. The TSCDY-BRB frame exhibits a mean IDR of about 0.40% (maximum of 0.54%), while the DY-BRB frame shows 0.33% (maximum of 0.44%). Hence, the peak drifts of the TSCDY-BRB frame are about 20–25% larger, and all values remain comfortably below 1%, satisfying typical life-safety criteria. The similar drift profiles indicate that the self-centering mechanism does not significantly alter the global deformation pattern.

A clear difference emerges in the residual deformations [Fig. 21(b)]. For the 0.2 g motions, the TSCDY-BRB frame exhibits negligible residual drifts, with a mean RIDR of about 5×10^{-6} and a maximum of 9×10^{-6}. In contrast, the DY-BRB frame develops mean and maximum RIDRs of about 4.8×10^{-5} and 6.6×10^{-5}, respectively. Thus, the residual drifts in the DY-BRB frame are nearly an order of magnitude larger than those of the TSCDY-BRB frame, so that the TSCDY-BRB residual drifts are roughly one-tenth of the DY-BRB values.

At the 0.4 g level, the mean and maximum RIDRs of the TSCDY-BRB frame increase to about 1.9×10^{-5} and 3.5×10^{-5}, while those of the DY-BRB frame reach 8.8×10^{-5} and 1.56×10^{-4}, respectively. Even at the MCE level, the TSCDY-BRB frame retains mean and maximum RIDRs about four to five times smaller than those of the DY-BRB frame. Moreover, the residual drifts of the TSCDY-BRB frame remain nearly uniform and very small across the height, while those of the DY-BRB frame concentrate in the upper stories.

To further illustrate brace behavior within the frame, Fig. 21(c)–(d) present the axial force–deformation hysteresis of the third-story braces under 0.2 g and 0.4 g El-Centro excitations. The DY-BRB braces develop wide bilinear loops with noticeable residual offsets, whereas the TSCDY-BRB braces exhibit flag-shaped loops with clear recentering and slightly slimmer loops. At 0.2 g, the TSCDY-BRB loops already show the onset of a second-stage yielding plateau, but the participation of the Group-2 cores remains limited; at 0.4 g this plateau becomes much more pronounced, indicating extensive engagement of the Group-2 cores. This evolution is consistent with the restoring-force model in Section 3 (Cases A and B), and further confirms that the intended self-centering double-stage mechanism is effectively mobilized in the frame at both DBE and MCE levels.

These results show that the restoring force provided by the tandem tendons is sufficient to overcome accumulated plastic deformations and drive the frame back toward its original position, while keeping peak inter-story drifts well within conventional design limits. Taken together with the component tests and parametric studies in Sections 3–5, the time-history analyses confirm that the TSCDY-BRB can deliver staged energy dissipation while markedly mitigating residual drift at the frame level.

6.4. Design implications for frame applications

The findings of this study provide practical implications for implementing TSCDY-BRBs in braced steel frames. At the component level, the brace should be proportioned so that the tendon prestress is not less than the total resistance of the two-stage energy-dissipation cores (including strain hardening), thereby maintaining a stable flag-shaped hysteresis and reliable recentering. At the system level, the six-story frame example indicates that, when the TSCDY-BRB frame is designed with initial stiffness and first-stage strength comparable to a DY-BRB frame, peak inter-story drifts remain of similar magnitude whereas residual drifts are markedly reduced under both DBE and MCE motions. These observations suggest that, by appropriately choosing prestress, staged strengths and preset gap, TSCDY-BRBs can provide combined self-centering and double-stage energy dissipation at different seismic intensity levels while keeping residual deformation under control in practical applications. A more comprehensive parametric study of brace–frame systems for different building heights and performance goals is left to future work.

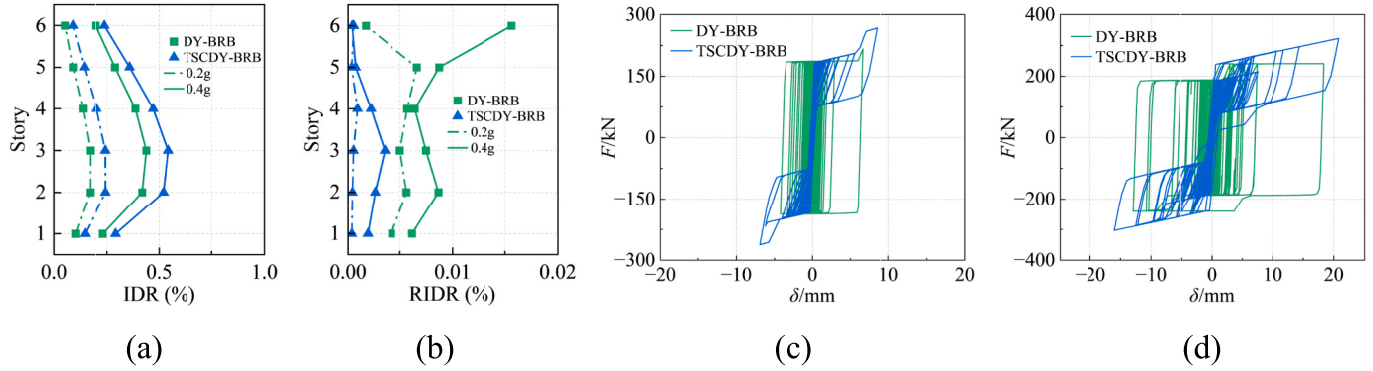

Fig. 21. System-level response comparison of frames with DY-BRBs and TSCDY-BRBs: (a) peak inter-story drift ratios, (b) residual inter-story drift ratios, (c)–(d) hysteresis of third-story braces under 0.2 g and 0.4 g El-Centro records, respectively.

7. Conclusions

This study proposes and validates a tandem self-centering double-stage yielding BRB (TSCDY-BRB), develops a staged-stiffness restoring-force model and a FE model, validates both against full-scale quasi-static tests, and conducts a parametric study to inform design.

1. The restoring-force model captures activation, Stage I and Stage II yielding, and re-engagement after about twice the preset gap, and clarifies when the second yield point to shift to the unloading branch. Together with the FE model, it reproduces the flag-shaped loops and stage transitions, with differences from tests within about 15%.
2. Across the examined ranges the brace maintains stable flag-shaped hysteresis. At the target amplitude, single-cycle energy is about 6.5–10.5 kJ, the equivalent viscous damping ratio is about 0.12–0.17, and the residual-to-peak displacement ratio can be kept below about 3% with adequate prestress and a moderate gap.
3. Prestress sets the strength baseline and recentering, with little effect on segmental tangent stiffness or single-cycle energy at a given amplitude. Strand diameter mainly tunes later-stage tangent stiffness while leaving initial strength nearly unchanged. The Group-1 core area governs Stage I, increases initial strength and stiffness, and markedly raises energy dissipation. The Group-2 core area governs Stage II, increases second-stage strength and stiffness, and adds high-amplitude energy once engaged. The preset gap controls Stage II engagement and re-engagement: larger gaps reduce loop fullness, energy dissipation and damping but improve recentering.
4. For design, use prestress to control recentering; choose strand diameter to tune later-stage stiffness; size Group-1 cores for low-amplitude strength and energy; size Group-2 cores for Stage II capacity and high-amplitude energy. Select the preset engagement gap together with the activation displacement and the Group-2 yield displacement so that their sum with twice the gap is below the target peak displacement, ensuring two-stage participation on both branches while balancing self-centering and energy dissipation.
5. System-level analyses show that, when the TSCDY-BRB frame is designed with the same initial stiffness and first-stage yield strength as a DY-BRB frame, it develops peak inter-story drifts of similar magnitude but much smaller residual inter-story drifts under 0.2 g and 0.4 g ground motions, demonstrating the effectiveness of the TSCDY-BRB for reparable frame design.

CRediT authorship contribution statement

Yongkang Kang: Writing – review & editing, Writing – original draft, Visualization, Validation, Project administration, Methodology, Formal analysis, Data curation, Conceptualization. **Bo Wen:** Writing – review & editing, Supervision, Resources, Project administration, Funding acquisition, Formal analysis, Conceptualization. **Shuaishuai Ji:** Visualization, Validation, Software, Methodology, Investigation, Formal analysis, Data curation, Conceptualization. **Alessio Fumagalli:** Writing – review & editing, Supervision. **Zhengyao Yu:** Investigation. **Wen Xia:** Investigation.

Declaration of competing interest

The authors declare that they have no known competing financial interests or personal relationships that could have appeared to influence the work reported in this paper.

Acknowledgement

This investigation received financial assistance from the National Natural Science Foundation of China (Grant No. 52078415), Scientific Research Fund of Institute of Engineering Mechanics, China Earthquake Administration (Grant No. 2020EEEVL0415), which is gratefully acknowledged.

Data availability

Data will be made available on request.

References

[1] Y. Zhou, H.T. Shao, Y.S. Cao, E.M. Lui, Application of buckling-restrained braces to earthquake-resistant design of buildings: a review, Eng. Struct. 246 (2021) 112991.
[2] Y. Zhou, W.B. Tian, Y. Xiao, Design recommendations for self-centering buckling restrained braces, Eng. Struct. 273 (2022) 115019.
[3] C.J. Black, N.M. Makris, I.D. Aiken, Component testing, seismic evaluation, and characterization of buckling-restrained braces, J. Struct. Eng. 130 (6) (2004) 880–894.
[4] R. Tremblay, Inelastic seismic response of steel bracing members, J. Constr. Steel Res. 58 (5–8) (2002) 665–701.
[5] R.A. Kersting, L.A. Fahnestock, W.A. López, Seismic Design of Steel Buckling-Restrained Braced Frames: A Guide for Practicing Engineers, NIST GCR 15–917-34, National Institute of Standards and Technology, Gaithersburg, MD, 2015.
[6] C. Christopoulos, R. Tremblay, H.J. Kim, M. Lacerte, Self-centering energy dissipative bracing system for the seismic resistance of structures: development and validation, J. Struct. Eng. 134 (1) (2008) 96–107.
[7] J. Erochko, C. Christopoulos, R. Tremblay, H.J. Kim, Shake-table testing and numerical simulation of a self-centering energy-dissipative braced frame, Earthq. Eng. Struct. Dyn. 42 (11) (2013) 1617–1635.
[8] L. Liu, J.X. Zhao, S. Li, Nonlinear displacement ratio for seismic design of self-centering buckling-restrained braced steel frame considering trilinear hysteresis behavior, Eng. Struct. 158 (2018) 199–222.
[9] Q. Xie, Z. Zhou, L.J. Huang, Influence of design load determination method for SC-BRBs with trilinear flag-shaped hysteresis behaviour on the seismic performance of braces and structures, Eng. Struct. 289 (2023) 116292.
[10] D.J. Miller, L.A. Fahnestock, M.R. Eatherton, Development and experimental validation of a nickel-titanium shape memory alloy self-centering buckling-restrained brace, Eng. Struct. 40 (2012) 288–298.
[11] C.C. Chou, P.T. Chung, Development of cross-anchored dual-core self-centering braces for seismic resistance, J. Constr. Steel Res. 101 (2014) 19–32.

[12] Y. Xiao, M.O. Eberhard, Y. Zhou, J.F. Stanton, J.H. Shen, Low-prestressing, self-centering energy-dissipative brace, Earthq. Eng. Struct. Dyn. 51 (12) (2022) 2837–2857.
[13] C.C. Chou, L.Y. Huang, Mechanics and validation tests of a post-tensioned self-centering brace with adjusted stiffness and deformation capacities using disc springs, Thin-Walled Struct. 195 (2024) 111430.
[14] P. Chen, L.H. Xu, S.X. Xie, Enhanced design and experimental investigation of disc spring-based self-centering buckling-restrained braces with a compounded combination mode, Earthq. Eng. Struct. Dyn. 52 (10) (2023) 3053–3073.
[15] L.H. Xu, X.W. Fan, Z.X. Li, Experimental behavior and analysis of self-centering steel brace with pre-pressed disc springs, J. Constr. Steel Res. 139 (2017) 363–373.
[16] L.H. Xu, X.W. Fan, Z.X. Li, Cyclic behavior and failure mechanism of self-centering energy dissipation braces with pre-pressed combination disc springs, Earthq. Eng. Struct. Dyn. 46 (7) (2017) 1065–1080.
[17] H.M. Zhang, L.M. Quan, X.L. Lu, Experimental hysteretic behavior and application of an assembled self-centering buckling-restrained brace, J. Struct. Eng. 148 (3) (2022) 04021302.
[18] C.Z. Zhang, S.J. Zhu, S.H. Zong, Z.G. Sui, X.N. Guo, Experimental and numerical investigations on an assembled self-centering buckling-restrained brace with high post-yield stiffness, Thin-Walled Struct. 190 (2023) 110927.
[19] W. Wang, C. Fang, Y.S. Zhao, R. Sause, S.L. Hu, J. Ricles, Self-centering friction spring dampers for seismic resilience, Earthq. Eng. Struct. Dyn. 48 (9) (2019) 1045–1065.
[20] O. Avsar, S.S. Cao, O.E. Ozbulut, Development and characterization of self-centering friction dampers with confined shape memory alloy bars, J. Build. Eng. 90 (2024) 109504.
[21] X. Yan, M.S. Alam, G.P. Shu, Y. Qin, A novel self-centering viscous damper for improving seismic resilience: its development, experimentation, and system response, Eng. Struct. 279 (2023) 115632.
[22] X. Yan, G.P. Shu, R.B. Zhang, M.S. Alam, Y. Qin, Hysteretic and seismic performance of disc spring-based self-centering viscous dampers for improved seismic resilience, Eng. Struct. 300 (2024) 117161.
[23] Y.K. Ding, M.K. Tang, M. Soy, Development and experimental verification for the coaxially formed self-centering buckling-restrained brace, J. Build. Eng. 73 (2023) 106525.
[24] X.S. Xie, L.H. Xu, Z.X. Li, Hysteretic model and experimental validation of a variable damping self-centering brace, J. Constr. Steel Res. 167 (2020) 105965.
[25] S.L. Hu, T. Guo, Y. Koetaka, Z.P. Chen, B. Wang, M.S. Alam, S.Y. Zhu, Seismic performance of hybrid self-centering braces with structural and nonstructural damage control functions: validation tests, computational modeling, and benefits evaluation, J. Struct. Eng. 151 (10) (2025) 04025163.
[26] G.Q. Li, Y.Z. Sun, J. Jiang, F.F. Sun, C. Ji, Experimental study on two-level yielding buckling-restrained braces, J. Constr. Steel Res. 159 (2019) 260–269.
[27] F. Barbagallo, M. Bosco, E.M. Marino, P.P. Rossi, Achieving a more effective concentric braced frame by the double-stage yield BRB, Eng. Struct. 186 (2019) 484–497.
[28] M.M. Jia, Y.Z. Chen, P.S. Jin, Development and validation analysis of a steel–lead hybrid dual-yield BRB for multi-stage seismic energy dissipation, Thin-Walled Struct. 199 (2024) 111822.
[29] B. Sitler, T. Takeuchi, R. Matsui, M. Suita, M. Terashima, Y. Terazawa, Experimental investigation of a multistage buckling-restrained brace, Eng. Struct. 213 (2020) 110482.
[30] W.Y. Wang, Y. Liu, Concept and performance testing of an all-steel miniature dual stiffness damper, J. Constr. Steel Res. 183 (2021) 106772.
[31] P. Pan, Y.R. Cao, H.S. Wang, J.B. Sun, Development of double-stage yielding coupling beam damper, J. Constr. Steel Res. 172 (2020) 106147.
[32] K.S. Dai, T.F. Sun, Y. Liu, T. Li, A. Camara, Concept and numerical analysis of a double-stage coupling damper for multilevel seismic protection, Thin-Walled Struct. 185 (2023) 110581.
[33] J.B. Sun, P. Pan, H.S. Wang, Development and experimental validation of an assembled steel double-stage yield buckling-restrained brace, J. Constr. Steel Res. 145 (2018) 330–340.
[34] B.L. Hu, Y.J. Min, C.H. Wang, Q. Xu, Y. Keleta, Design, analysis and application of the double-stage yield buckling restrained brace, J. Build. Eng. 48 (2022) 103980.
[35] J.C. Wang, J.J. Men, Q. Zhang, D.X. Fan, S.X. Qi, C.H. Huang, Cyclic behavior of a shape-optimized dumbbell-type combined slit damper with phased yielding characteristic, J. Build. Eng. 88 (2024) 109216.
[36] Z. Zhang, S.N. Zhang, E.F. Deng, T.T. Zhou, Y. Yi, H. He, N.N. Li, Experimental study on seismic performance of double-level yielding buckling-restrained braced concrete frames, Arch. Civ. Mech. Eng. 20 (2020) 44.
[37] C.Z. Zhang, X.N. Guo, Y.H. Zhao, Y. Liu, Development of an innovative assembled self-centering dual-stage yield buckling-restrained brace for improving seismic resilience, Eng. Struct. 329 (2025) 119804.
[38] H. Jiang, L.H. Xu, X.S. Xie, P. Chen, Seismic behavior of double activation self-centering brace and braced structures, J. Struct. Eng. 149 (7) (2023) 04023082.
[39] C. Chen, W.H. Zhong, Z. Tan, X. Zhang, W.H. Fang, S.C. Duan, Research on hysteretic behavior of self-centering brace with staged yield energy dissipation, Structures 76 (2025) 108945.
[40] Y. Yang, J.Y. Xue, L. Zheng, R. Liu, Manufacturing, testing and simulation of novel dual stage energy-dissipation and self-centering friction damper, J. Constr. Steel Res. 222 (2024) 108949.
[41] H. Azizi, P. Lehner, M. Eghbali, J. Ahmadi, B. Badarloo, Performance assessment of novel parallel double-stage yield buckling-restrained braces for seismic hazard mitigation, J. Constr. Steel Res. 227 (2025) 109389.
[42] Q. Xie, Z. Zhou, J.H. Huang, D.P. Zhu, S.P. Meng, Finite-element analysis of dual-tube self-centering buckling-restrained braces with composite tendons, J. Compos. Constr. 21 (3) (2017) 04016112.
[43] R. Rahnavard, M. Naghavi, M. Aboudi, M. Suleiman, Investigating modeling approaches of buckling-restrained braces under cyclic loads, Case Stud. Constr. Mater. 8 (2018) 476–488.
[44] Y. Qing, C.L. Wang, Z. Zhou, B. Zeng, Seismic responses of multistory buildings with self-centering buckling-restrained braces: influence of the pretension force, Eng. Struct. 238 (2021) 112249.
[45] P. Chen, L.H. Xu, Z.X. Li, Study on prediction method of initial stiffness of self-centering energy dissipation braces, Eng. Struct. 247 (2021) 113226.
[46] C.X. Qiu, S.Y. Zhu, High-mode effects on seismic performance of multi-story self-centering braced steel frames, J. Constr. Steel Res. 119 (2016) 133–143.
[47] ABAQUS, Analysis User's Manual-Version, ABAQUS INC, USA, 2020.
[48] L.J. Jia, R.W. Li, P. Xiang, D.Y. Zhou, Y. Dong, Resilient steel frames installed with self-centering dual-steel buckling-restrained brace, J. Constr. Steel Res. 149 (2018) 95–104.
[49] GB 50011–-2010, Code for Seismic Design of Buildings, Standards Press of China, 2010.